

# Controlled doping of ultralow amounts Ru on Ni cathode for PEMWE: Experimental and theoretical elucidation of enhanced performance

Kyeong-Rim Yeo<sup>a,1</sup>, Hoyoung Kim<sup>b,1</sup>, Kug-Seung Lee<sup>c</sup>, Seongbeen Kim<sup>b</sup>, Jinwoo Lee<sup>b,\*</sup>, Haesun Park<sup>a,\*</sup>, Soo-Kil Kim<sup>a,\*</sup>

<sup>a</sup> School of Integrative Engineering, Chung-Ang University, Seoul 06974, Republic of Korea

<sup>b</sup> Department of Chemical and Biomolecular Engineering, Korea Advanced Institute of Science and Technology (KAIST), Daejeon 34141, Republic of Korea

<sup>c</sup> Pohang Accelerator Laboratory, Pohang 37673, Republic of Korea

## ARTICLE INFO

### Keywords:

Electrodeposition  
Ni-Ru catalyst  
Hydrogen evolution reaction  
Proton exchange membrane water electrolyzer

## ABSTRACT

Proton exchange membrane water electrolysis (PEMWE) is an environmentally benign technology for large-scale hydrogen production. Despite many catalysts being developed to replace Pt, successful development of low-cost catalysts that meet the balance of performance and durability is limited. In this work, atomically dispersed Ru on Ni catalyst-integrated porous transport electrodes were fabricated by a simple electrodeposition. With a trace amount of Ru ( $< 0.05 \text{ mg}_{\text{Ru}}\text{-cm}^{-2}$ ), the  $\text{Ni}_{98.1}\text{Ru}_{1.9}$  cathode catalyst exhibited an overpotential of 35 mV at  $-10 \text{ mA}\cdot\text{cm}^{-2}$  with excellent stability. Density functional theory calculation revealed that the high performance was driven by optimized adsorption strength and improved mobility of hydrogen on the catalyst surface. The  $\text{Ni}_{98.1}\text{Ru}_{1.9}$  electrode was further verified in a PEMWE cell and resulting performance ( $6.0 \text{ A}\cdot\text{cm}^{-2}$  at  $2.25 \text{ V}_{\text{cell}}$ ) and stability ( $0.13 \text{ mV}\cdot\text{h}^{-1}$  decay rate at  $1 \text{ A}\cdot\text{cm}^{-2}$ ) surpassed previously reported non-Pt and even Pt electrodes, demonstrating its readiness as an advanced cathode to replace Pt.

## 1. Introduction

Water electrolysis coupled with renewable energy sources such as solar, hydro, and wind energy is considered as a promising eco-friendly technology producing green hydrogen [1,2]. Compared to traditional alkaline water electrolysis (AWE), proton exchange membrane water electrolysis (PEMWE) provides several benefits including compactness, low gas permeability, high purity gas production, high stability, low ohmic loss, and high current density [3,4]. Moreover, it is considered as the most appropriate electrolysis technology adaptable to variable or intermittent renewable energy to secure grid stability [2,5]. However, the exorbitant cost of membrane electrode assembly (MEA) with costly Pt and Ir catalysts limits its large-scale industrial commercialization [6]. Unfortunately, catalysts for oxygen evolution reactions occurring at potentials higher than  $1.23 \text{ V}_{\text{RHE}}$  are restricted to extremely scarce Ir-based catalysts. Therefore, researchers seek to reduce the quantity of Ir necessary in oxygen electrodes without sacrificing performance [7–11]. On the other hand, there is room for dramatic reduction in the cost of PEMWE by applying earth-abundant non-Pt materials as the

cathode because the hydrogen evolution reaction (HER) occurs below  $0 \text{ V}_{\text{RHE}}$ , which is a reductive environment [12–16].

Accordingly, the possibility of using non-Pt materials as HER catalysts in PEMWE have been extensively explored, taking into consideration the correlation between the Gibbs free energy for hydrogen adsorption ( $\Delta G_{\text{H}}$ ) on the catalyst surface and the corresponding HER activity [16,17]. As a result, inexpensive transition metals (TMs) such as Ni, Co, Mo, W, and Cu have emerged as potential candidates [13]. However, non-Pt single metal catalysts are not efficient due to their 2–5 orders of lower exchange current density compared with Pt [17]. In order to improve the catalytic activity of non-Pt materials, TM alloys [18,19], phosphides [16,20], chalcogenides [21,22], carbides [23], and nitrides [24] have been used to obtain a favorable electronic structure, which affects  $\Delta G_{\text{H}}$ . Accordingly, recent studies focus on finetuning the electronic structure of Ni because Ni has the most appropriate  $\Delta G_{\text{H}}$  of  $-0.27$  to  $-0.23 \text{ eV}$  among the single TMs [14,19,25–37].

To enhance the catalytic activity and stability of Ni for the acidic conditions of HER, alloys with Mo, W, Co, and Cu have been proposed [19,25–31]. In particular, NiMo and NiW, which are combinations of Ni

\* Corresponding authors.

E-mail addresses: [jwlee1@kaist.ac.kr](mailto:jwlee1@kaist.ac.kr) (J. Lee), [parkh@cau.ac.kr](mailto:parkh@cau.ac.kr) (H. Park), [sookilkim@cau.ac.kr](mailto:sookilkim@cau.ac.kr) (S.-K. Kim).

<sup>1</sup> These authors contributed equally to this work.

with internally paired *d*-electrons and Mo or W with half-empty *d*-orbitals, showed a high performance with a low overpotential of 20–70 mV at  $-10 \text{ mA cm}^{-2}$ , which is comparable to that of Pt (20–40 mV) [25–28]. However, their limited durability still remained as an obstacle. Studies to improve durability have been conducted on compound catalysts such as Ni phosphides [14,32,33], chalcogenides [34], carbides [35,36], and nitrides [36,37] to secure a high chemical stability. However, their performance (overpotential of 60–300 mV at  $-10 \text{ mA cm}^{-2}$ ) is still insufficient to compete with the highly active Pt due to its poor electrical conductivity and insufficient active sites [14,32–37]. These observations confirm once again that the properties of activity and durability are not easily compatible with each other.

Despite the substantial advances in non-precious HER catalysts, the above-mentioned limitations of moderate activity and limited durability inspire finding new alternatives. Ru, for example, has a hydrogen bond strength close to that of Pt [38] and has recently emerged as a promising candidate material for both alkaline [39,40] and acidic HER [38,41–46]. For the efficient utilization of Ru, nanoparticles dispersed on carbon (Ru-HPC [41], Ru@C<sub>2</sub>N [42]), Ru-based alloy (RuCo@CD [43], Mo@Ru [44]), and compound (RuP<sub>2</sub>@NPC [45], RuTe<sub>2</sub>-M [46]) catalysts with regulated electronic structures have been investigated, demonstrating excellent performance and stability comparable to those of Pt. However, the continuous increase in industrial demand for Ru increases its price, and even if it is half the price of Pt currently [47], research on the reduction of Ru usage is important.

Another issue in the development of TM-based HER is that most studies are limited to the half-cell test under three-electrode configuration, with just a few investigations of feasibility at a single cell level [12]. Solution-based half-cell and MEA type zero-gap single cell systems have substantial discrepancies from the construction of catalyst/electrode to operating conditions, so the high performance and durability in half-cell experiments are not necessarily guaranteed in MEA-based single cell [48,49]. Therefore, it is crucial both to design highly active, durable, and efficient electrocatalysts and to validate their practical feasibility by fabricating MEA to conduct a single cell test under harsher and realistic operating conditions [12,48–50].

Herein, we aimed to suggest a novel HER catalyst and propose a method for its fabrication to catch the best of both the activity and durability with a thorough verification at the single cell level, which can be directly applicable to the commercial PEMWE system. We synthesized binder-free catalyst-integrated porous transport electrodes (PTEs) that can be directly applicable to the MEA fabrication for PEMWE. Trace amounts of Ru-doped Ni was fabricated on carbon paper (CP) by electrodeposition, which is a fast process that can be completed within minutes at room temperature and atmospheric pressure without using hazardous raw materials [51,52]. The intrinsic poor HER activity of Ni was drastically improved by Ru doping, resulting in an optimized  $\Delta G_{\text{H}}$  and facile surface diffusion of adsorbed hydrogen confirmed by the density functional theory (DFT) calculation. The exceptionally high activity and durability of the Ru-doped Ni catalyst were experimentally verified both at the half-cell and single-cell levels. By doping of Ru on the surface of Ni at 2 at%, the PEMWE performance and durability obtained with the developed cathode were superior to those of non-Pt electrodes and comparable to or even higher than those of Pt electrodes reported previously, clearly demonstrating the readiness of the material and fabrication method for the commercial PEMWE system.

## 2. Experimental section

### 2.1. Preparation of catalysts

The Ni, Ru, and Ru-doped Ni catalysts were fabricated by electrodeposition using a potentiostat (Metrohm, Autolab, PGSTAT302N) in a three-electrode cell system. Carbon paper (CP; Ballard, Avcarb MGL280), graphite rod (WonATech, GR002H), and saturated calomel electrode (SCE, CHI Instruments, CHI150) were used as the working

electrode, counter electrode, and reference electrode, respectively. Before electrodeposition, carbon paper was functionalized with hydrophilic groups through sonication in dilute HNO<sub>3</sub> solution (60 wt%) for 15 min [53]. For the electrodeposition, NiCl<sub>2</sub>·6 H<sub>2</sub>O (Wako pure chemical industry, 141-01045) and RuCl<sub>3</sub>·H<sub>2</sub>O (Alfa Aesar, 11043) as sources of Ni and Ru, respectively, were dissolved in deionized (D.I., 18.2 M $\Omega$ ) water. NH<sub>4</sub>Cl (Daejung, 1060-4100) was added to allow for the precise control of Ru content by replacing Ru aqua-chloro complex into amine-chloro ligand form, which is harder to reduce [54]. Also, HCl was used to increase the acidity of the electrolyte, and H<sub>3</sub>BO<sub>3</sub> (Daejung, 2036-4405) was added as a buffer agent to maintain the electrolyte pH during electrodeposition accompanied by hydrogen evolution to prevent the metal ions from forming hydroxide precipitates [55]. Then, the solution was purged with N<sub>2</sub> for 30 min to remove dissolved O<sub>2</sub>. The Ni-Ru catalysts were fabricated by applying a constant potential of  $-1.7 \text{ V}_{\text{SCE}}$  for 10 min on the CP with an exposed area of  $1 \text{ cm}^2$  to the electrolyte. For comparison, Ru<sub>100</sub> catalyst was also electrodeposited under the same conditions except a longer deposition time of 30 min due to the limited reduction rate of Ru complex in the absence of Ni precursor. The electrodeposited catalysts were then heat-treated under 5% H<sub>2</sub>/Ar atmosphere at 200 °C for 2 h with a heating rate of  $10 \text{ }^\circ\text{C min}^{-1}$  to increase the stability in acidic water electrolysis electrolyte. The doping level of Ru in Ni-Ru catalysts was finely tuned by controlling the molar concentration of Ru precursor in a range of 0.5–5 mM while maintaining that of the Ni precursor. Detailed electrodeposition conditions are summarized in Table 1.

### 2.2. Material characterizations

Field emission scanning electron microscopy (FE-SEM, Sigma, Carl Zeiss) was performed to observe the surface morphology of the prepared catalysts. The bulk atomic composition and the loading amount of the element were analyzed by inductively coupled plasma mass spectrometry (ICP-MS, NexION300, PerkinElmer). The same was used in the analysis of dissolved catalysts after the stability test. The bulk crystal structure of the prepared catalyst was analyzed by X-ray diffraction (XRD, New D8-Advance, Bruker-AXS) at a rate of  $2^\circ \text{ min}^{-1}$  in a range of 30–80°. The valence state and atomic coordination were confirmed by X-ray absorption near edge structure (XANES), which was measured at 8 C nano-probe X-ray absorption fine structure (XAFS) beamline of the Pohang Light Source (PLS-II) with a 3.0 GeV storage ring under a ring current of 250 mA. The higher-order harmonics were eliminated by monochromating the X-ray beam using a Si (111) double crystal with a 30% decrease in beam intensity. The beam size of the X-ray was then modified as 0.5 mm (v)  $\times$  1 mm (h) when it was supplied to a secondary source aperture. The modes of transmission or fluorescence were used to gather the XANES spectra. The Demeter package was used to process the collected spectra. The Artemis software was used to fit Fourier transformed  $k^2$ -weighted extended X-ray absorption fine structure (EXAFS) spectra. The electronic structure and oxidation state of the surface were analyzed by X-ray photoelectron spectroscopy (XPS, K-alpha+, ThermoFisher Scientific). For the obtained XPS spectra, the C 1s region was calibrated to a binding energy of 284.8 eV. XPS was also used to measure the valence band spectra (VBS), the higher level of integration was set at 15.0 eV for the Shirley background removal, and the intensity of the highest peak was calibrated to be equal [56]. To prevent any alteration in surface-sensitive analysis by possible precipitations between Ru and NH<sub>4</sub>Cl-containing HCl solution [57], electrochemical cleaning of samples in 0.5 M H<sub>2</sub>SO<sub>4</sub> solution was applied for 3 times prior to XPS and X-ray absorption spectroscopy. The cleaning step was determined to be identical to the HER activity test conditions to avoid any impact on the catalyst performance, which was confirmed by no change in HER performance during initial 10 potential cycling.

**Table 1**  
Electrodeposition conditions of catalysts and the metal loading amounts measured by ICP-MS.

Bulk atomic composition by ICP-MS	Electrolyte configuration / mM					Deposition potential / $V_{SCE}$	Deposition time / min	Loading amount / $mg\ cm^{-2}$	
	NiCl <sub>2</sub>	RuCl <sub>3</sub>	H <sub>3</sub> BO <sub>3</sub>	NH <sub>4</sub> Cl	HCl			Ni	Ru
Ni <sub>100</sub>	50	0	300	100	10	- 1.7	10	2.346	-
Ni <sub>99.7</sub> Ru <sub>0.3</sub>	50	0.5						3.020	0.015
Ni <sub>98.9</sub> Ru <sub>1.1</sub>	50	2						1.774	0.034
Ni <sub>98.1</sub> Ru <sub>1.9</sub>	50	5						1.350	0.046
Ru <sub>100</sub> - 10 min	0	5						-	0.004
Ru <sub>100</sub> - 30 min	0	5					30	-	0.058

### 2.3. Computational methods

DFT calculations were performed as implemented in the Vienna ab initio simulation package (VASP) [58,59]. The projected-augmented wave (PAW) potential was employed to describe the core-valence electron interactions [60,61]. The plane-wave basis set with a cutoff energy of 520 eV was used to describe valence electrons. The Perdew–Burke–Ernzerhof (PBE) generalized gradient approximation (GGA) was used to treat the exchange-correlation functionals [62]. The spin-polarized calculations were performed in all computations. The k-points were generated by the Python Materials Genomics (pymatgen) code with a density of at least 1200/reciprocal atom ( $21 \times 21 \times 21$  for bulk and  $7 \times 7 \times 1$  for slab) [63]. A surface structure model of Ni (111)-( $2\sqrt{3} \times 2\sqrt{3}$ )R30° with four layers was used, and each slab model was separated from its neighbors by a sufficiently thick vacuum layer ( $\sim 15 \text{ \AA}$ ). One hydrogen atom was absorbed on the surface. During the surface structure relaxation, only the top two layers were allowed to move, while the bottom two layers were fixed. For hydrogen-absorbed structures, only the hydrogen atom was allowed to relax. All calculations were relaxed to an atomic force tolerance of  $0.03 \text{ eV \AA}^{-1}$ . The Ru dopant atoms were distributed into the surface (1/3, 2/3, and 1 ML) and subsurface (4/3, 5/3, and 2 ML) layers (Fig. S21). A Bader charge analysis was performed to analyze the charge transfer between Ni and Ru dopants [64,65]. The hydrogen diffusion barriers were calculated by taking the total energy difference between the fcc hollow site and the bridge/atop site. When hydrogen atom was not stable at the bridge or atop sites, the climbing image nudged elastic band (NEB) method was used [66]. A force tolerance of  $0.05 \text{ eV \AA}^{-1}$  was used for NEB calculations.

### 2.4. Electrochemical measurements

The activity of the prepared catalysts on HER was confirmed by cyclic voltammetry (CV) measurement in 0.5 M H<sub>2</sub>SO<sub>4</sub> solution using a three-electrode cell system, where SCE was used as a reference electrode, and a graphite rod was used as a counter electrode instead of Pt to avoid the dissolution of Pt counter electrode and subsequent HER signal from the re-deposited Pt on the working electrode. For comparison, commercial Ru black catalyst (Sigma Aldrich, 326712) with a loading amount of 0.1 mg of Ru per cm<sup>2</sup> and Pt/C catalyst (Alfa Aesar, 47308) with the same loading amount of 0.1 mg of Pt per cm<sup>2</sup> were also tested through spray coating of catalyst ink solutions on carbon paper. The ink solution for Ru black was composed of Ru black, D.I. water, isopropanol, and Nafion® D-520 dispersion (Alfa Aesar, 042118) at a weight ratio of 9:50:236:20, while that for Pt/C was composed of Pt/C, D.I. water, IPA, and Nafion® D-520 dispersion at a weight ratio of 5:50:157:36. The CV was measured at a scan rate of  $5 \text{ mV s}^{-1}$  in a range of 0.02 to  $-0.33 V_{RHE}$ . Accelerated degradation test (ADT) for HER was performed with 1000 cycles at a scan rate of  $100 \text{ mV s}^{-1}$  over the same range. In addition, the stability test was evaluated at  $-10 \text{ mA cm}^{-2}$  for 24 h. The potential in the polarization curves was converted to a reversible hydrogen electrode (RHE), and iR-correction was performed by measuring the ohmic resistance obtained with electrochemical

impedance spectroscopy (EIS, Wuhan Corrtest Instruments Corp. Ltd., CS310). To compare the electrochemical surface areas of the catalysts, the electrochemical double layer capacitance ( $C_{dl}$ ) was measured in a designated potential range by varying the scan rate in a range of  $20\text{--}100 \text{ mV s}^{-1}$  in 1 M NaOH solution. Before the experiments, the solution was purged with N<sub>2</sub> for 30 min to remove dissolved O<sub>2</sub>.

### 2.5. Membrane electrode assembly (MEA) preparation and single cell operation

For the preparation of MEA, Ni-Ru/CP with the highest HER activity observed in half-cell experiments was applied to a cathode. No further treatment such as binder coating was made on the electrodeposited cathode. As an anode, commercial IrO<sub>x</sub> with 2.0 mg of Ir per cm<sup>2</sup> was spray-coated on CP, Ti fiber felt (Bekaert), and Pt-coated Ti fiber felt (Bekaert) to restrain the performance degradation induced by Ti oxidation [67,68] with a catalyst ink composed of IrO<sub>x</sub> powder (Alfa Aesar, 043396), D.I. water, isopropanol (IPA), and Nafion® D-520 dispersion at a weight ratio of 9:50:236:20. For comparison, commercial Pt/C with 0.05 and 0.1 mg of Pt per cm<sup>2</sup> were prepared by spray-coating on carbon paper to be used as cathodes, and the Pt/C ink was composed of Pt/C (Alfa Aesar, 47308), D.I. water, IPA, and Nafion® D-520 dispersion at a weight ratio of 5:50:157:36. Nafion® 212 (DuPont, 50.8- $\mu\text{m}$  thick) and Nafion® 115 (DuPont, 127- $\mu\text{m}$  thick) were used as proton exchange membrane. Before use, Nafion 115 membrane was continuously immersed in 3 wt% H<sub>2</sub>O<sub>2</sub> at 80 °C for 1 h, 0.5 M H<sub>2</sub>SO<sub>4</sub> at 80 °C for 1 h, and D.I. water at 80 °C for 1 h, and stored in D.I. water at room temperature. The active area of MEA was fixed at  $1 \times 1 \text{ cm}^2$ . During the PEMWE operation, the temperature of the cell was maintained at 90 °C, and preheated D.I. water was only supplied to the anode side at a rate of  $15 \text{ ml min}^{-1}$  through the line heater at a fixed temperature of 95 °C. After activation at  $2.3 V_{cell}$  for 20 min, the performance of water electrolyzer was evaluated by applying a cell voltage ranging from 2.3 to  $1.35 V_{cell}$  at intervals of 50 mV. The duration time at each voltage was 1 min. Single cell stability test was conducted for 100 h at  $1 \text{ A cm}^{-2}$ . EIS measurement was performed to subdivide the overpotentials in the PEMWE performance curves using a potentiostat (Metrohm, Autolab, PGSTAT302N) at  $1 \text{ A cm}^{-2}$  in a frequency range of 100 kHz to 10 Hz with an amplitude of  $10 \text{ mA cm}^{-2}$ .

## 3. Results and discussion

### 3.1. Synthesis and characterizations of Ni-Ru electrodes

A scheme of the preparation process of Ni-Ru catalyst-integrated PTE is shown in Fig. 1a. First, CP substrate was treated in a HNO<sub>3</sub> solution to increase the hydrophilicity of the surface to facilitate subsequent electrodeposition. Then, the catalyst was simply fabricated through electrodeposition under the conditions described in Table 1 and heat-treated in a 5% H<sub>2</sub>/Ar atmosphere at 200 °C for 2 h to enhance its stability. The surface morphology of the carbon paper and electrodeposited Ni-Ru catalysts (with heat-treatment) was observed by FE-SEM (Fig. 1b–g). The carbon fiber constituting the carbon paper showed a smooth surface

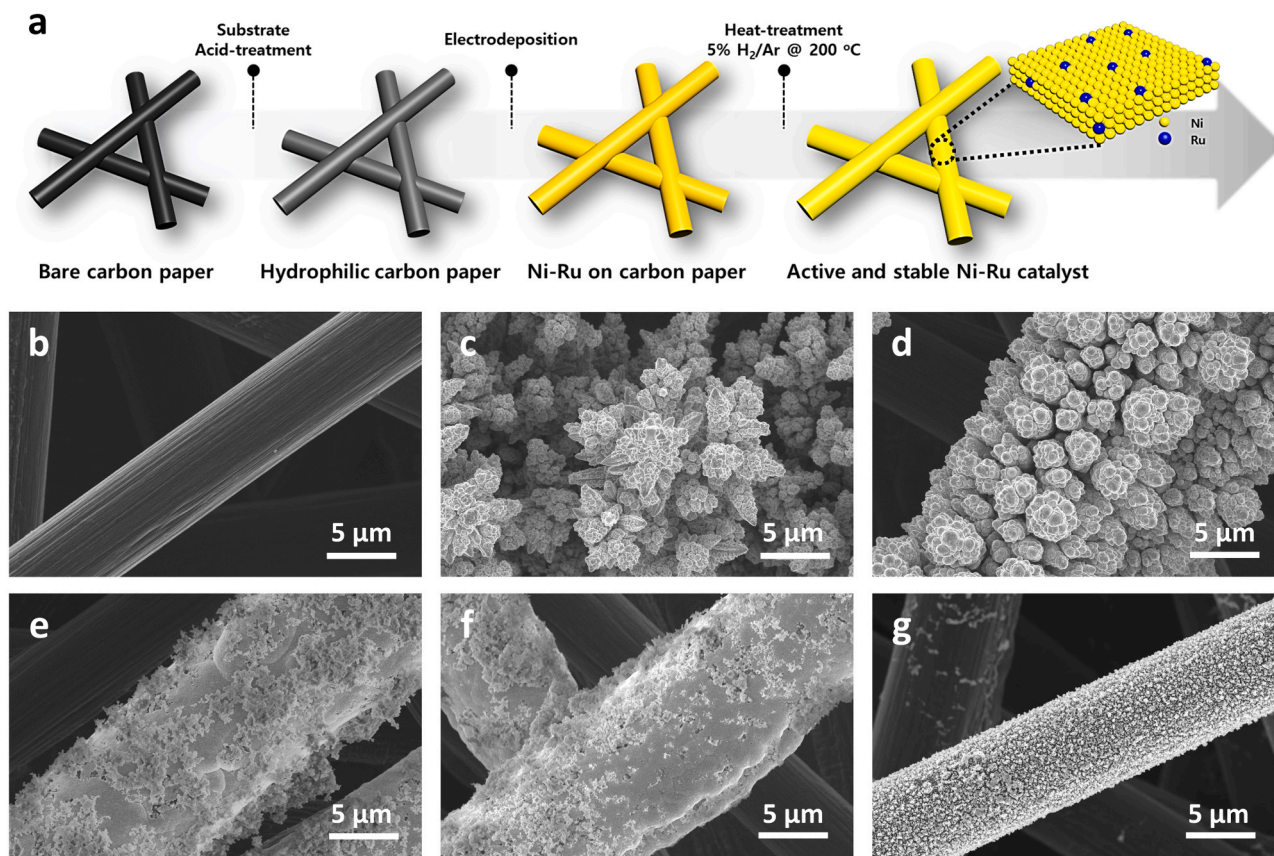


**Fig. 1.** (a) Schematic illustration of the preparation of Ni-Ru catalyst. FE-SEM images of (b) bare carbon paper, (c) Ni<sub>100</sub>, (d) Ni<sub>99.7</sub>Ru<sub>0.3</sub>, (e) Ni<sub>98.9</sub>Ru<sub>1.1</sub>, (f) Ni<sub>98.1</sub>Ru<sub>1.9</sub>, and (g) Ru<sub>100</sub> samples electrodeposited on carbon paper. All electrodeposited samples were heat-treated.

(Fig. 1b). Ni<sub>100</sub> catalyst (Fig. 1c) exhibited radially grown dendritic deposits with a rough surface due to the mass transfer-limited electrodeposition at a highly negative deposition potential of  $-1.7$  V<sub>SCE</sub> and H<sup>+</sup> supplied from NH<sub>4</sub><sup>+</sup> participating in hydrogen evolution [69]. On the other hand, the Ni<sub>100</sub> deposit in NH<sub>4</sub>Cl-free electrolyte showed a smooth surface (Fig. S1a). The Ni<sub>99.7</sub>Ru<sub>0.3</sub> catalyst with the smallest Ru content (Fig. 1d) seemed to have somewhat smoother edges and more uniform deposits compared with Ni<sub>100</sub>, likely because Ru and NH<sub>4</sub>Cl in the HCl electrolyte formed a complex [54] to reduce the deposition kinetic and make the deposition be less controlled by mass transfer of the precursors. Further addition of Ru precursor in the deposition bath resulted in a higher incorporation of Ru in the deposits (Ni<sub>98.9</sub>Ru<sub>1.1</sub> in Fig. 1e and Ni<sub>98.1</sub>Ru<sub>1.9</sub> in Fig. 1f), inducing a significant change in the deposition morphology from dendritic clusters to film-like structures due to the substantial inhibition of the deposition through complex formation. The inhibition of the deposition is further observed in the decrease in the loading amounts for those samples confirmed by ICP-MS analysis in Table 1. The poor deposition efficiency by the complex formation was ultimately seen in the case of Ru<sub>100</sub> with 10 min deposition (Fig. S1b), resulting in uniformly scattered Ru nano particles and a limited loading quantity of 0.004 mg cm<sup>-2</sup> (Table 1). In contrast, when the amine complex was not formed, the deposition kinetic was enhanced (Fig. S1c). The deposition time for Ru<sub>100</sub> was extended to 30 min (Fig. 1g) to approximate the amount of Ru loading in Ni<sub>98.1</sub>Ru<sub>1.9</sub> (Table 1) for comparison. Note that heat treatment at 200 °C for 2 h had no significant effect on the morphologies of the samples (Fig. S2). On the carbon paper, the electrodeposited catalysts were produced uniformly, but the physically deposited powder-type Ru catalyst (Fig. S3a) was distributed quite randomly with irregularly shaped particles.

The crystal structures of the prepared Ni-Ru catalysts were analyzed by XRD (Fig. 2a). Carbon paper, used as a substrate, was also compared.

In the case of carbon paper, several peaks were observed at 43.02, 44.67, and 54.79°, which correspond to the (101), (102), and (008) planes of carbon (JCPDS #26-1080), respectively. In the Ni<sub>100</sub> deposit, clear Ni peaks indicating the (111), (200), and (220) planes with a face-centered cubic (fcc) crystal structure (JCPDS #04-0850) were observed at about 44.51, 51.85, and 76.4° along with the peaks of carbon paper. With the introduction of Ru, the position of the Ni peaks remained unchanged, but their intensity progressively decreased, and the full width at half maximum (FWHM) became wider. Using Scherrer equation with the FWHM for a peak at 44.51°, the crystalline size of the catalysts was calculated (Fig. 2b). The crystallite size of Ni<sub>100</sub> was about 31.5 nm, but it was reduced to 27.5 nm when 0.3 at% of Ru was added, and sharply decreased to 18.3 nm when the Ru content was increased to 1.1 at%. Ru aqua-chloro complex in RuCl<sub>3</sub>·H<sub>2</sub>O precursor was replaced into amine-chloro ligand form when NH<sub>4</sub>Cl was added in the electrolyte, which is harder to reduce [54]. Formation of this complex results in the inhibition of the facile deposition, thus, the growth of crystalline structure of Ni has retarded as observed in Fig. S1b and S1c. Further increase in Ru content (1.9 at%) slightly decreased the crystalline size to about 17.3 nm. It should be also noted that no Ru peaks were observed regardless of the Ru content in Ni-Ru or Ru<sub>100</sub> catalysts. While the Ru powder with a loading of 0.1 mg cm<sup>-2</sup> shows clear crystallinity (Fig. S3b), Ru<sub>100</sub> shows no observable peaks, indicating a nanocrystalline or an amorphous structure. Therefore, in the case of Ni-Ru, the amount of Ru incorporated during the electrodeposition was insufficient to form either a crystalline structure or a bulk alloy with Ni.

In order to understand the valence state and local coordination structure of Ni and Ru at the atomic level in the Ni-Ru catalyst, Ni K-edge and Ru K-edge of acid-treated Ni<sub>98.1</sub>Ru<sub>1.9</sub> (Fig. S4) with the highest Ru content was conducted with X-ray absorption spectroscopy (XAS) (Fig. 2c-f; normalized curves). For a more precise interpretation of the

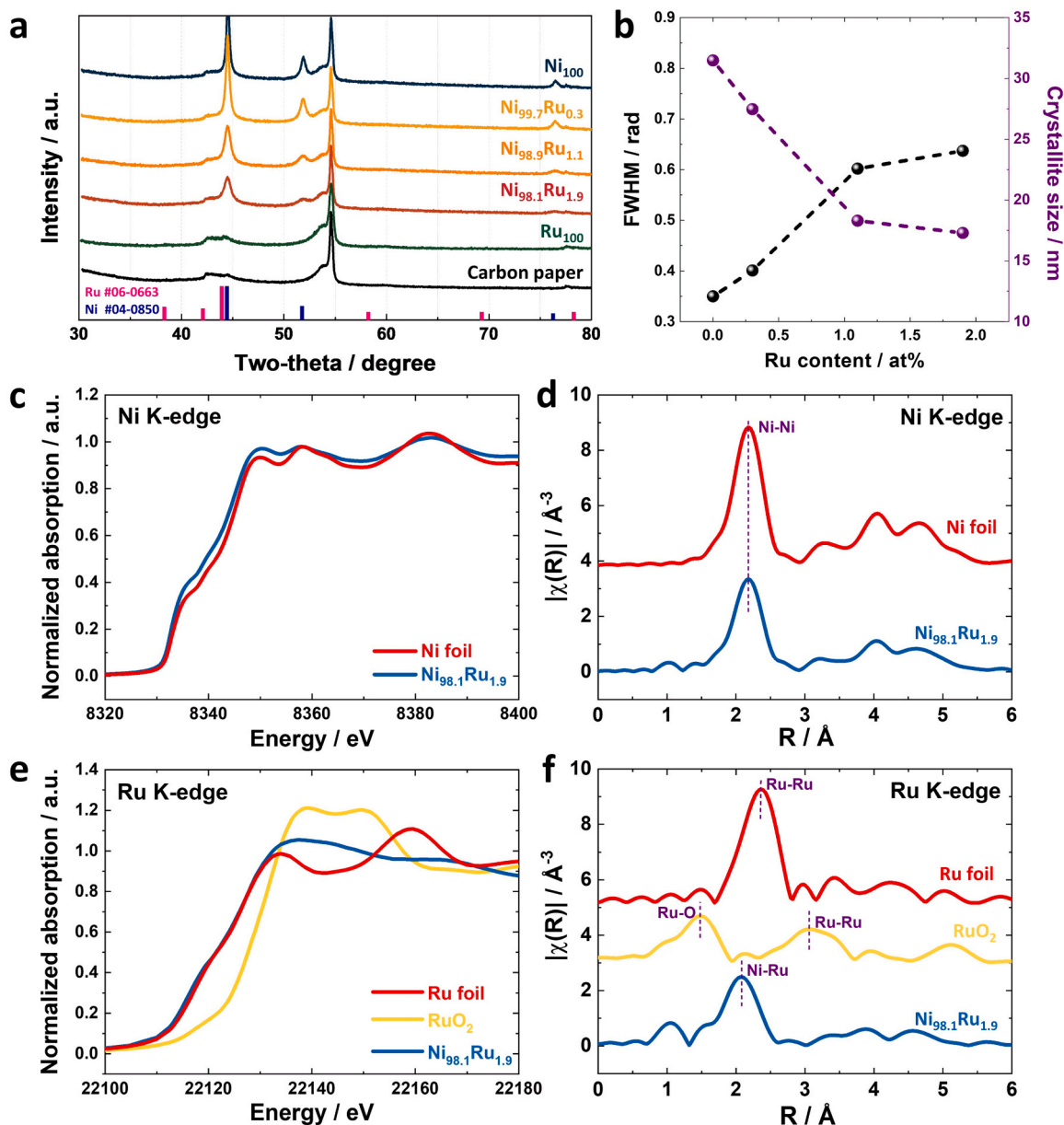


**Fig. 2.** (a) XRD patterns of bare carbon paper and electrodeposited  $\text{Ni}_{100}$ ,  $\text{Ni}_{99.7}\text{Ru}_{0.3}$ ,  $\text{Ni}_{98.9}\text{Ru}_{1.1}$ ,  $\text{Ni}_{98.1}\text{Ru}_{1.9}$ , and  $\text{Ru}_{100}$  samples. Solid markers at the bottom indicate the fcc Ni (navy) and hcp Ru (pink). (b) FWHM and crystallite size according to atomic concentration of Ru. (c) XANES and (d) EXAFS spectra at Ni K-edge for Ni foil and  $\text{Ni}_{98.1}\text{Ru}_{1.9}$ . (e) XANES and (f) EXAFS spectra at Ru K-edge for Ru foil,  $\text{RuO}_2$ , and  $\text{Ni}_{98.1}\text{Ru}_{1.9}$ .

coordination environment, EXAFS fitting was performed (Fig. S5 and S6), and the fitted parameters were presented in Table S1 and S2. The edge of  $\text{Ni}_{98.1}\text{Ru}_{1.9}$  was similar to that of Ni foil (Fig. 2c), reflecting the metallic state of Ni in  $\text{Ni}_{98.1}\text{Ru}_{1.9}$ . In the corresponding Fourier transformed EXAFS profiles (Fig. 2d), Ni-Ni coordination was confirmed at the same position as the Ni foil at  $\sim 2.2$  Å with a slight decrease in peak intensity for  $\text{Ni}_{98.1}\text{Ru}_{1.9}$ , which was caused by decrease in the coordination number (CN) from 12 to 7.97 as Ni-Ru was nanocrystallized by Ru doping, consistent with the XRD results (Fig. 2a). In Ru K-edge XANES (Fig. 2e), the edge of  $\text{Ni}_{98.1}\text{Ru}_{1.9}$  was also located very close to Ru foil, which demonstrates that the Ru atoms in  $\text{Ni}_{98.1}\text{Ru}_{1.9}$  was in a metallic state. In the FT-EXAFS profiles for Ru (Fig. 2f), Ru-Ru coordination was located at  $\sim 2.4$  Å in Ru foil, and Ru-O at  $\sim 1.5$  Å and Ru-Ru at  $\sim 3.1$  Å in  $\text{RuO}_2$ , whereas in  $\text{Ni}_{98.1}\text{Ru}_{1.9}$ , a prominent peak was observed at  $\sim 2.1$  Å, indicating that the Ru in  $\text{Ni}_{98.1}\text{Ru}_{1.9}$  had a coordination environment different from that in Ru foil. EXAFS fitting shows that the interatomic distance of Ru-Ni in  $\text{Ni}_{98.1}\text{Ru}_{1.9}$  is  $2.51$  Å, which is

slightly longer than that of Ni-Ni ( $2.48$  Å) as shown in Table S1 and S2 due to the larger atomic size of Ru than that of Ni. It also indicates that the CN (6.88) is less than that of Ni-Ni, implying that Ru is more exposed on the surface. In addition, the wavelet transform was plotted for distinguishing the type of coordinated atom for atomically dispersed Ru (Fig. S7). Since wavelet transform can resolve the  $k$  dependence of EXAFS, it is fine tool to distinguish the Z of coordinating atom, even they are at the similar distance (R) from the central atom [70]. When the type of central atom is Ru, wavelet transform of Ru and  $\text{RuO}_2$  represent the maximum at  $k$  value of  $\sim 9$  Å $^{-1}$ . However,  $\text{Ni}_{98.1}\text{Ru}_{1.9}$  (when the central atom is Ru) has maximum at different  $k$  value of  $\sim 8$  Å $^{-1}$ , indicating that the Z value of backscattering atom for  $\text{Ni}_{98.1}\text{Ru}_{1.9}$  is different from the Ru and  $\text{RuO}_2$  (Their backscattering atom is Ru) (Fig. S7 a-c, e). When the type of central atom is Ni, wavelet transform of Ni represent the maximum at  $k$  value of  $\sim 7.5$  Å $^{-1}$ . Also, the  $\text{Ni}_{98.1}\text{Ru}_{1.9}$  (when the central atom is Ni) has maximum at  $k$  value of  $\sim 7.5$  Å $^{-1}$ . These results indicate that the backscattering atom for both Ni and Ru in  $\text{Ni}_{98.1}\text{Ru}_{1.9}$  is not Ru

but Ni, indicating that Ru is atomically dispersed without forming agglomerates. In conclusion, these results indicated that Ru species in  $\text{Ni}_{98.1}\text{Ru}_{1.9}$  were atomically dispersed without forming the Ru agglomerates and they were stabilized by coordination of  $\sim 7$  Ni atoms with bond length of 2.51 Å.

### 3.2. Electrochemical measurements

The activity for acidic HER of the Ni-Ru catalysts was evaluated in 0.5 M  $\text{H}_2\text{SO}_4$  (Fig. 3). The HER polarization curves in Fig. 3a showed that the  $\text{Ni}_{100}$  catalyst had negligible activity with an overpotential of 171 mV to reach  $-10 \text{ mA cm}^{-2}$ . As 0.3 at% of Ru is doped to Ni ( $\text{Ni}_{99.7}\text{Ru}_{0.3}$ ), the overpotential to obtain  $-10 \text{ mA cm}^{-2}$  was substantially decreased to 46 mV. As the doping level of Ru was further increased to 1.1 and 1.9 at%, the overpotential further decreased to 36 and saturated to 35 mV. After that, as the Ru content were further increased, the overpotential were also increased to 46 mV for  $\text{Ni}_{95.2}\text{Ru}_{4.8}$  and 47 mV for  $\text{Ni}_{88.8}\text{Ru}_{11.2}$ , respectively (Fig. S8a), of which the reason will be explained in the DFT calculation section. These values are superior to those of non-precious catalysts (51–183 mV) and low precious

catalysts (35.7–125 mV) except those of  $\text{Ru}@C_2\text{N}$  (22 mV; 0.082 mg of Ru per  $\text{cm}^2$ ),  $\text{MoRu}_3$  (30.5 mV; 0.21 mg of Ru per  $\text{cm}^2$ ) catalysts with relatively large loadings of Ru (Fig. 3c, Table S3–4), and commercial Pt/C (5 mV; 0.1 mg of Pt per  $\text{cm}^2$ ) that has been tested for comparison. Considering that the extremely small amounts of Ru doping to Ni resulted in a superior activity compared with  $\text{Ru}_{100}$  catalyst (42 mV) and Ru black (134 mV), the outstanding activity of Ni-Ru catalyst is due to the modification of H adsorption energy by Ru doping, which will be further discussed in the coming DFT section.

To confirm the mechanism for HER, a Tafel plot was generated (Fig. 3b) using the polarization curves presented in Fig. 3a. For the  $\text{Ni}_{100}$  catalyst, Tafel slope is highest to be  $134 \text{ mV dec}^{-1}$  indicating that the Volmer step ( $120 \text{ mV dec}^{-1}$ ) of proton adsorption on the catalyst surface served as a rate determining step (RDS). Ru black had a Tafel slope of  $93 \text{ mV dec}^{-1}$ , suggesting that the Volmer reaction also occurred rather slowly. It might be more plausible to correlate the high Tafel slopes of 93 and  $134 \text{ mV dec}^{-1}$  measured at this low overpotential to Volmer-RDS [71]. However, a more complex effect of surface hydrogen coverage on the Tafel slope leaves a possibility that those high slopes around  $120 \text{ mV dec}^{-1}$  are the results of Heyrovsky-RDS [72]. As we have no

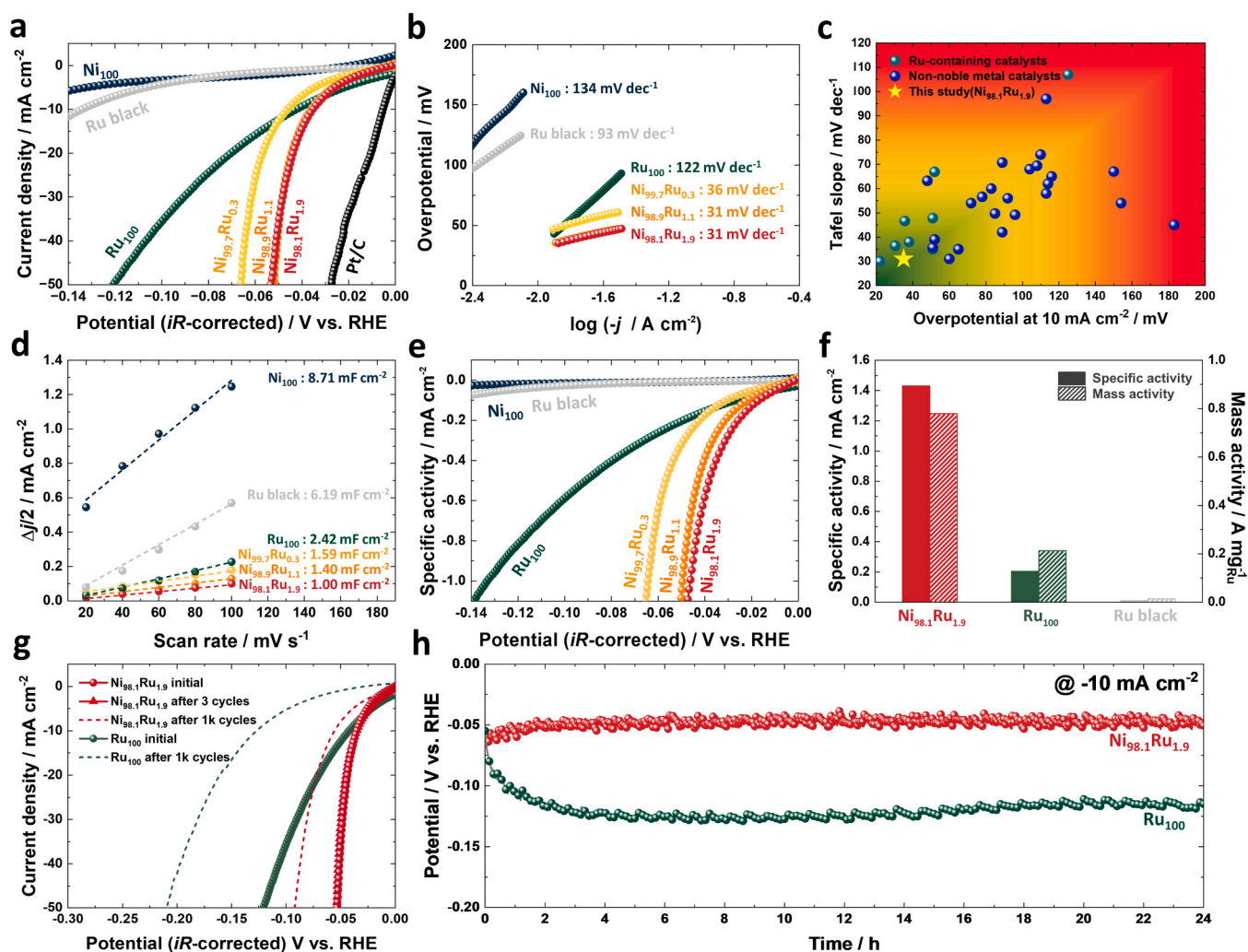


**Fig. 3.** Electrochemical characterizations. (a) HER polarization curves of electrodeposited  $\text{Ni}_{100}$ ,  $\text{Ni}_{99.7}\text{Ru}_{0.3}$ ,  $\text{Ni}_{98.9}\text{Ru}_{1.1}$ ,  $\text{Ni}_{98.1}\text{Ru}_{1.9}$ ,  $\text{Ru}_{100}$ , and Ru black powder measured at a scan rate of  $5 \text{ mV s}^{-1}$  with iR-compensation. (b) Tafel plots derived from the HER polarization curves of the corresponding catalysts. (c) Performance comparison with literature-reported catalysts in Table S3 and S4. (d) Electrochemical double layer capacitance ( $C_{dl}$ ). (e) Specific activity. (f) Histogram of specific activity and mass activity for  $\text{Ni}_{98.1}\text{Ru}_{1.9}$ ,  $\text{Ru}_{100}$ , and Ru black at an overpotential of 50 mV. (g) Accelerated degradation test (ADT) for 1000 cycles at a scan rate of  $100 \text{ mV s}^{-1}$ . A polarization curve after acid treatment (3 cycles) was also presented showing no change in the HER performance. (h) Chronopotentiometry of  $\text{Ni}_{98.1}\text{Ru}_{1.9}$  and  $\text{Ru}_{100}$  at  $-10 \text{ mA cm}^{-2}$  for 24 h (without iR-compensation). All electrochemical measurements except those in (d) were performed in the 0.5 M  $\text{H}_2\text{SO}_4$  electrolyte at room temperature.

further information on the surface hydrogen coverage on those catalysts, it is more appropriate to suggest the possibility of both Volmer-RDS and Heyrovsky-RDS on Ni and Ru black than to definitely conclude the mechanism. However, for the highly active (fast kinetic) Ru-doped Ni and Ru<sub>100</sub>, no clear Tafel relationships were observable at overpotential higher than 120 mV due to the early occurrence of mass transfer limitation. Instead, the Tafel regions for those catalysts were formed in the low overpotential region where the current for the reverse reaction might not be negligible. Therefore, in those cases, to perform the Tafel analysis using the low overpotential data, an alternative equation suggested by Allen and Hickling [73] applicable to quasi-reversible system [74] was adopted. In the case of Ru<sub>100</sub>, the Tafel slope was measured to be 122 mV dec<sup>-1</sup>. Doping of a small amount of Ru (0.3 at%) to Ni resulted in a rapid decrease in Tafel slope from that of Ni (134 mV dec<sup>-1</sup>) to 36 mV dec<sup>-1</sup>, which is significantly lower than that of Ru<sub>100</sub> by 86 mV dec<sup>-1</sup> and close to the theoretical value of the Heyrovsky step (40 mV dec<sup>-1</sup>). This implies that the RDS on this catalyst is the reaction between the protons adsorbed on the surface and the protons in the electrolyte to produce H<sub>2</sub>. This also suggests that there is a synergistic effect when Ru is doped to Ni. As Ru content gradually increased to 1.1 and 1.9 at%, the Tafel slope for those catalysts decrease to 31 mV dec<sup>-1</sup>, meaning that the RDS of HER on those catalysts change from Heyrovsky step to Tafel step. The Tafel step with the theoretical slope of 30 mV dec<sup>-1</sup> involves the two adsorbed protons combined with each other to form H<sub>2</sub>. Drastic decreases in the Tafel slopes on Ni<sub>98.9</sub>Ru<sub>1.1</sub> and Ni<sub>98.1</sub>Ru<sub>1.9</sub> suggest that the adsorption/desorption strength of H on those catalysts was optimized. As the Ru contents were further increased to 4.8 and 11.2 at%, the Tafel slopes were also increased to 79 and 98 mV dec<sup>-1</sup>, respectively (Fig. S8b). The activity of best performing Ni<sub>98.1</sub>Ru<sub>1.9</sub> was compared with the reported Ni-based catalysts in Fig. 3c and Table S3 in terms of Tafel slope and overpotential at -10 mA cm<sup>-2</sup>. It showed that our Ni<sub>98.1</sub>Ru<sub>1.9</sub> catalyst outperforms most of the reported catalysts in terms of both the kinetics and required energy.

One of the major factors that can affect the catalytic activity is the electrochemical surface area of the catalyst. To examine this effect, the electrochemical double layer capacitance (C<sub>dl</sub>) of Ni-Ru catalysts was measured by changing the scan rate in 1 M NaOH solution (Fig. S9), and the results are presented in Fig. 3d. It is recommended to use alkaline electrolyte for non-noble catalysts when measuring C<sub>dl</sub> [28,33] because there is no non-faradaic region in the acidic solution due to the dissolution of Ni. The surface area was compared by dividing the obtained C<sub>dl</sub> by the specific capacitance (C<sub>s</sub>) of 40 μF cm<sup>-2</sup> to obtain the roughness factor [75]. The Ni<sub>100</sub> had a large roughness factor of 217.75, reflecting the vertically grown structures, as seen in the FE-SEM image in Fig. 1c. The roughness factor of Ni<sub>99.7</sub>Ru<sub>0.3</sub> rapidly decreased to 39.75, reflecting the smoother surface. As the content of Ru further increased, the roughness factor gradually decreased to 35 for Ni<sub>98.9</sub>Ru<sub>1.1</sub>, and to 25 for Ni<sub>98.1</sub>Ru<sub>1.9</sub>, but to a rather large value of 60.5 for Ru<sub>100</sub>, which is in good accordance with the morphology trend shown in Fig. 1. To compare the intrinsic activity of the catalysts excluding the surface area effect, the specific activity was calculated (Fig. 3e) by dividing the geometric current density of polarization curve for HER in Fig. 3a by the roughness factor of each catalyst obtained from Fig. 3d. As a result, it presented a similar trend to the geometric current density (Fig. 3a), and Ni<sub>98.1</sub>Ru<sub>1.9</sub> still showed the highest specific activity. From the specific activity (Fig. 3e) and Ru mass activity (Fig. S10), the performance at an overpotential of 50 mV for Ni-Ru and Ru was compared in Fig. 3f. Ni-Ru exhibited 7.01-fold and 169.4-fold higher specific and 3.66-fold and 59.7-fold higher mass activities than those of Ru<sub>100</sub> and Ru black, respectively, demonstrating its outstanding efficiency.

The stability of the catalyst was verified in two ways. For durability evaluation, an accelerated degradation test (ADT) was performed for 1000 cycles at a scan rate of 100 mV s<sup>-1</sup> in the same potential range of HER evaluation (Fig. 3g). After ADT, Ni<sub>98.1</sub>Ru<sub>1.9</sub> only displayed a 20 mV rise in overpotential at 10 mA cm<sup>-2</sup>, from 35 to 55 mV, but Ru<sub>100</sub> had a significant degradation of 85 mV, from 42 to 127 mV, demonstrating the

advantageous effect of Ru atom on the stability of the catalyst. To evaluate the long-term durability of the best-performing Ni<sub>98.1</sub>Ru<sub>1.9</sub>, and Ru<sub>100</sub> in comparison, a cathodic current density of 10 mA cm<sup>-2</sup> was applied for 24 h and the potential profile was observed over time (Fig. 3h). As clearly shown in the figure, the initial overpotential of 64 mV (iR-uncompensated) was slightly decreased to 48 mV after 24 h exhibiting extremely good stability. After durability test, SEM, XRD, C<sub>dl</sub>, and XPS analyzes were performed and presented in Fig. S11. In addition, ICP-MS analysis was performed for the electrolyte during the durability test. There was no significant change in the crystal structure, electronic structure, and surface composition (Ni<sub>96</sub>Ru<sub>4</sub>) in the XRD pattern (Fig. S11b) and XPS (Fig. S11e and S11f). However, from the ICP-MS analysis of the electrolyte (Fig. S12), there was a gradual dissolution of the catalyst components, particularly Ni, within the first 12 h of the durability test and then remained stable thereafter. As a result, the surface morphology was changed to be more porous (Fig. S4a vs. Fig. S11a) and the corresponding C<sub>dl</sub> was increased from 1.00 to 6.72 mF cm<sup>-2</sup> after the durability test (Fig. S11c to d), which is responsible for the increase in the activity after the durability test. However, Ru<sub>100</sub> catalysts exhibited a drastic increase in the overpotential with a decay rate of 2.5 mV h<sup>-1</sup> implying its poor durability.

### 3.3. Origin of electrocatalytic enhancement

The electronic structure of Ni after Ru doping was investigated through XPS analysis, and the atomic structure of Ni-Ru was interpreted using the results. Representatively, Ni<sub>100</sub>, Ru<sub>100</sub>, and Ni<sub>98.1</sub>Ru<sub>1.9</sub> were examined (Fig. 4). Ni<sub>100</sub> and Ru<sub>100</sub> were mostly present in the metallic state. After Ru was doped in Ni, the Ni surface was mostly in an oxidized state because Ni-Ru has a strong H<sub>2</sub>O and OH adsorption. On the other hand, due to the higher electronegativity of Ru (2.2) compared with Ni (1.91), Ru in Ni-Ru received electrons from Ni and showed a peak at 461.76 eV, a negative shift of 0.16 eV compared to Ru<sub>100</sub> (461.92 eV). In addition, the area of each peak in the XPS spectra was divided by the corresponding Relative Sensitivity Factors (RSF) to confirm the elemental presence on the surface. The surface element ratio through XPS quantitative analysis is Ni<sub>96</sub>Ru<sub>4</sub>, where the Ru content was slightly higher than the bulk element ratio of Ni<sub>98.1</sub>Ru<sub>1.9</sub> measured by ICP-MS. This indicates that most of Ru was exposed on the surface of the Ni-Ru catalyst due to the segregation enthalpy of Ru in Ni-Ru alloy (-4 kJ mol<sup>-1</sup>) [76]. In addition, since the acidic HER performance is closely related to the *d*-band center of the catalyst in terms of its electron densities in bonding and anti-bonding states, the *d*-band center of the catalysts was experimentally analyzed through XPS valence band spectra. As shown in Fig. 4c, with the increase in Ru doping level in Ni, the *d*-band center shifted away from the Fermi level, confirming that the adsorption strength of H atom was weakened.

Combining the EXAFS and XPS results, it was concluded that the Ru atoms were predominantly well dispersed on the surface Ni structure. In order to understand the underlying mechanism behind the increased HER activity of the Ni catalyst when doped with Ru, we modeled the Ni structure with preferential Ru doping on the surface/subsurface and performed DFT calculations to elucidate the effect of Ru doping on the HER activity and the electronic structure of the Ni-Ru catalyst. We also vary the amount of Ru at the surface/subsurface region to gain insight into the effect of Ru concentration to the HER activity. The HER activity of Ni catalyst is known to be hindered by the strong adsorption of H atom on Ni surfaces with an adsorption energy (ΔE<sub>H</sub>) of -0.53 eV. Our DFT calculations revealed that H adsorption to the surface becomes weaker upon Ru doping on the Ni surface. Fig. 5a shows that the adsorption energy (blue line) decreases as the concentration of Ru doping at the surface increases. When Ru fully covers the very surface of Ni (1 ML), the adsorption energy reaches its minimum value (-0.34 eV), which is comparable to Pt catalyst (-0.33 eV) [17]. However, when Ru is further infiltrated into the subsurface region as depicted in Fig. 5b, the trend is reversed, and the H adsorption becomes stronger with subsurface Ru

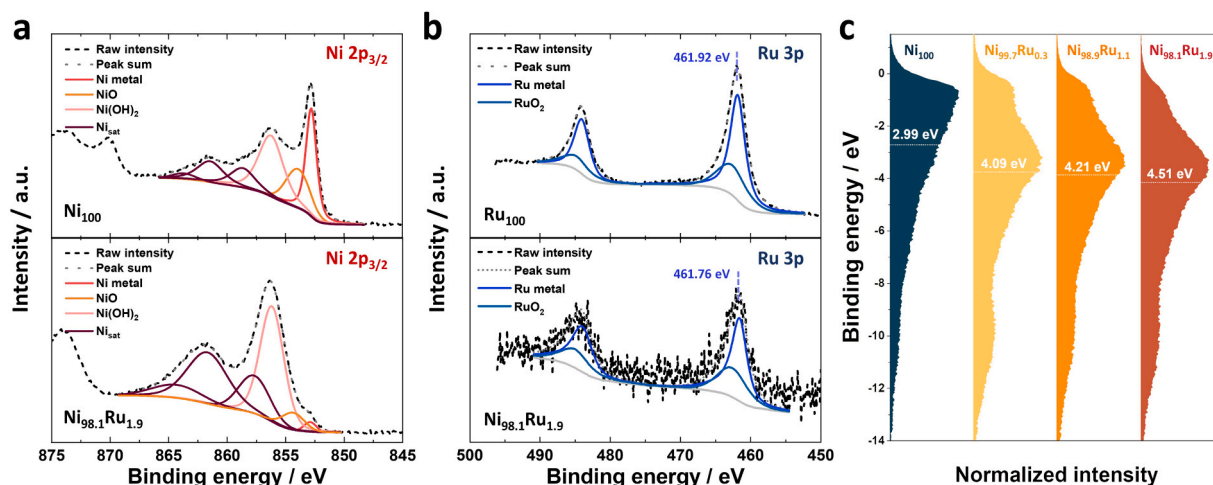


Fig. 4. XPS spectra of (a) Ni  $2p_{3/2}$  and (b) Ru  $3p$  for  $\text{Ni}_{100}$ ,  $\text{Ni}_{98.1}\text{Ru}_{1.9}$ , and  $\text{Ru}_{100}$ . The raw intensity is represented with a short black dash, and obtained fitting is presented with a gray dotted line. (c)  $d$ -band center position experimentally estimated from the normalized valence band spectra (VBS) of  $\text{Ni}_{100}$ ,  $\text{Ni}_{99.7}\text{Ru}_{0.3}$ ,  $\text{Ni}_{98.9}\text{Ru}_{1.1}$ , and  $\text{Ni}_{98.1}\text{Ru}_{1.9}$ .

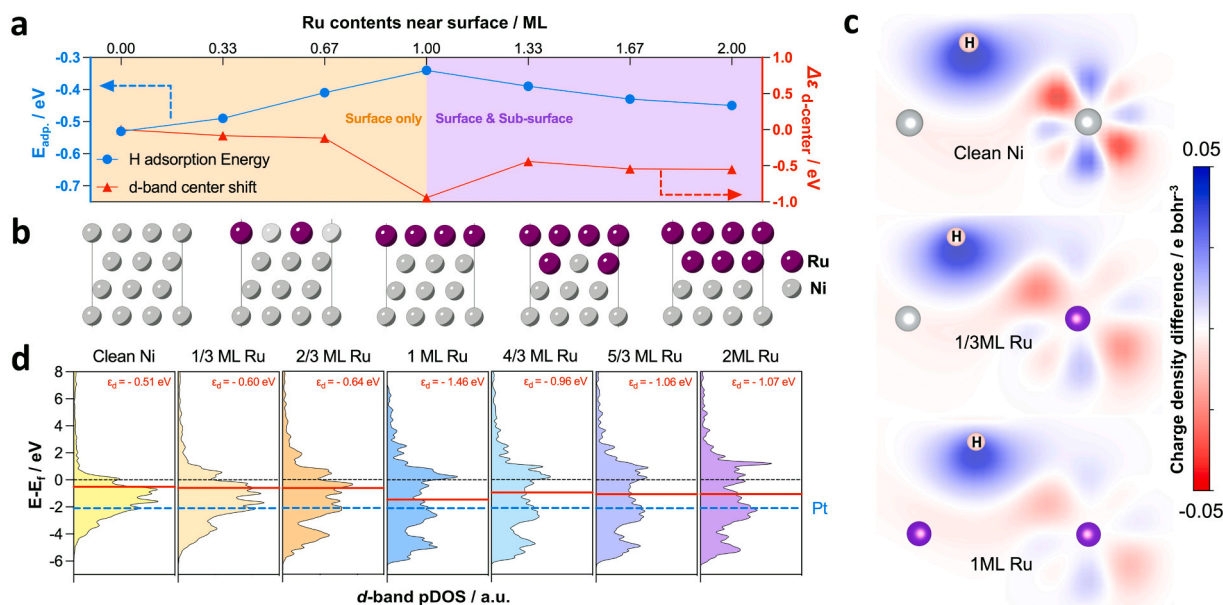


Fig. 5. (a) H adsorption energies (blue) and the shift in  $d$ -band center with respect to clean Ni surface (red). The abscissa is the amount of Ru coverage on the Ni surface. (b) Schematic atomic structure of Ru doped Ni surface. (c) Charge density difference,  $\rho_{\text{adsorbed}} - \rho_{\text{isolated}}$ , for H adsorbed on clean Ni (top), 1/3 ML Ru (middle), and 1 ML Ru (bottom) catalyst. Red shading represents charge accumulation due to H-TM interaction (maximum charge density =  $0.05 \text{ e bohr}^{-3}$ ), and blue area corresponds to charge depletion (minimum charge density =  $-0.05 \text{ e bohr}^{-3}$ ). (d) The projected density of  $d$ -band state. Red annotation is the  $d$ -band center of the surface atoms. The solid red and dotted blue lines represent the position of  $d$ -band center of Ni-Ru and Pt surface, respectively.

concentration. When the Ru content near the surface reaches 2 MLs, getting close to Ru bulk, the adsorption energy rises back to  $-0.45 \text{ eV}$ . This explains the volcano trends in HER performance according to Ru contents in Fig. S8. However, the weaker adsorption (relative to clean Ni surface) is maintained in all cases, which is in good accordance with the HER performances in Fig. 3a. The reduced interaction between H and Ru atoms can be also seen from the H adsorbed structures (Fig. S13), where the H-Ru bond length ( $1.79\text{--}2.12 \text{ \AA}$ ) is generally larger than the H-Ni bond ( $1.70\text{--}1.72 \text{ \AA}$ ).

The variation in adsorption ability with respect to Ru concentration is consistent with the trend in charge density accumulation/depletion map between H adsorbate and catalyst surface (Fig. 5c). For clean Ni surface, large degrees of charge accumulation and depletion are observed near Ni and H atoms, respectively, implying a strong

interaction between the adsorbate and catalyst. Upon 1/3 ML Ru doping, the degree of charge accumulation reduced not only near the Ru atom (Fig. 5c, middle), but also near the Ni atom (Fig. S14). The minimum charge accumulation was observed at 1 ML Ru where the lowest adsorption energy was observed. Interestingly, the degree of charge accumulation rises back at 2 ML Ru (Fig. S15), which follows the adsorption energy trend.

The H adsorption ability of the catalyst can be understood through its electronic structure, especially the  $d$ -band center level,  $\epsilon_d$ . We can estimate the degree of occupation of the anti-bonding state from  $\epsilon_d$  and consequently the adsorption strength. If  $\epsilon_d$  is high (close to Fermi energy), the less anti-bonding state is occupied, resulting in a strong adsorption ability and vice versa [77,78]. Fig. 5d shows the projected density of state (DOS) of the surface layer of clean and Ru-doped Ni



catalysts. The results shown in Fig. 5d suggest the dependency of  $\epsilon_d$  on the Ru doping concentration, and the  $\epsilon_d$  trend is in accordance with the adsorption energy variation. The clean Ni surface had an  $\epsilon_d$  of  $-0.51$  eV and, as Ru was doped on the surface,  $\epsilon_d$  shifts down. When Ru fully covers the Ni surface,  $\epsilon_d$  reaches the minimum ( $-1.46$  eV). However, as the Ru atoms are infiltrated into the subsurface,  $\epsilon_d$  jumps to around  $-1.00$  eV and no significant variation is observed with further increase in Ru concentration. The variation in  $\epsilon_d$  with respect to Ru concentration is consistent with those measured from XPS (Fig. 4c) and as well with the trend of calculated energies for H adsorption (Fig. 5a), where the lower the  $\epsilon_d$ , the weaker the adsorption strength.

The lowest  $\epsilon_d$  is observed when Ru fully covers the surface of Ni catalyst (1 ML), and this is associated with the synergetic effects of compressive strain and electron transfer [17,79]. The Ru atoms with large radius experience the compressive strain on the Ni substrate whose radius is relatively smaller than Ru, lowering the  $\epsilon_d$ . Also, the Bader charge analysis has shown that 0.42 e of charge is transferred from Ni substrate to Ru overlayer. The additional electron widens the bandwidth of Ru  $d$ -band to maintain the band-filling, inducing the  $\epsilon_d$  shift-down. However, the addition of Ru atoms to the subsurface region raises  $\epsilon_d$  due to the charge redistribution over the subsurface region. The attracted charge from Ni is distributed to not only over the surface Ru but also over the subsurface Ru, reducing the amount of additional charge from Ni to the surface Ru region. This is evidenced by Bader charge analysis, where the amount of charge transferred to the surface Ru was reduced to 0.30–0.35 e at 4/3–2 ML. This indicates that the over-rutheniation can adversely affect the HER activity by re-strengthening the H adsorption ability back to Ni, and our results pinpoint that the performance would be optimized when 1 ML of Ru overlayer covers the Ni catalyst.

To comprehensively understand the electronic structure in different Ru-doped Ni catalyst surface models, the adsorption energies and the  $d$ -band center shift with respect to the Ru concentration are also plotted in Fig. S16(a) for models where the subsurface layer is initially doped with Ru, followed by introducing Ru dopant at the outermost surface, as illustrated in Fig. S16(b). In this model, compared to the Ni surface without Ru doping, the adsorption ability increases with rising Ru concentration up to 1 ML. However, once the outermost surface begins to be filled, there is a significant decrease in adsorption ability. The shift in the  $d$ -band center corresponds to the adsorption energy trend, where a higher  $d$ -band center corresponds to a stronger adsorption strength. The catalyst with Ru concentrations equal to or lower than 1 ML exhibits stronger adsorption strength compared to the clean Ni catalyst. Conversely, the adsorption strength of the catalyst with Ru

concentrations greater than 1 ML, where the outermost surface is doped, is weaker than that of the clean Ni catalyst. Combining the results from the two different models, it is evident that the enhanced HER activity implies the presence of outermost Ru doping.

The reduced interaction between H adsorbate and catalyst surface also enhances the mobility of surface H. The H atom on the surface is most stable on the 3-fold hollow sites, fcc hollow (f site in Fig. 6a) and hcp hollow (h site in Fig. 6a), where the H atom diffuses on the surface through hopping between these two sites [80]. There are two pathways of hopping between the hcp and fcc sites, where H migrates either through the 2-fold bridge site (b site in Fig. 6a) or the 1-fold atop site (a site in Fig. 6a). For clean Ni surface, the H migration through the bridge site has an energy barrier of 0.11 eV (Pt: 0.05 eV), while the migration through the atop site on Ni surface is quite sluggish with an energy barrier of 0.56 eV (Pt: 0.10 eV), allowing a limited H diffusion compared with the Pt surface [80]. Our calculations revealed that Ru doping generally facilitates the H diffusion on Ni catalyst surface for the bridge and atop site diffusion paths. Fig. 6b summarizes the diffusion barriers through the bridge and atop sites (Ni and Ru atop sites). The diffusion through the bridge sites exhibits a relatively small variation ( $\sim 0.05$  eV) in activation energy. At Ru 1 ML, where the weakest adsorption occurs, the energy barrier for H migration through the bridge decreases as well to 0.09 eV and the corresponding diffusivity ( $\sim e^{-E_b/k_B T}$ , at 300 K and assume the same pre-factor) is one-third of that of Pt. At Ru 1 ML, the migration barrier through the atop site is greatly reduced to 0.34 eV which corresponds to orders of magnitude increase in diffusivity compared with clean Ni surface. Despite the large degree of reduction in energy barrier for atop site migration, however, the diffusivity is approximately five-order of magnitude higher in migration through bridge site, indicating that the path through the bridge site still dominates H diffusion. Still, the reduced migration barrier through the bridge site improves the overall H diffusion on the catalyst and consequent HER activity.

### 3.4. PEM electrolyzer performance

Conclusively, the significant HER improvement of Ru-doped Ni catalyst at half-cell evaluation is mostly due to the optimized H-binding/diffusion when small amounts of Ru are preferentially and uniformly distributed on the surface of Ni-Ru catalysts. To guarantee that the high performance of Ni-Ru catalysts is maintained at the PEMWE single cell level, the single cell performance was evaluated by applying the  $\text{Ni}_{98.1}\text{Ru}_{1.9}$  catalyst, which had the best performance in HER half-cell evaluation, as the cathode of PEMWE operating at 90 °C in the voltage

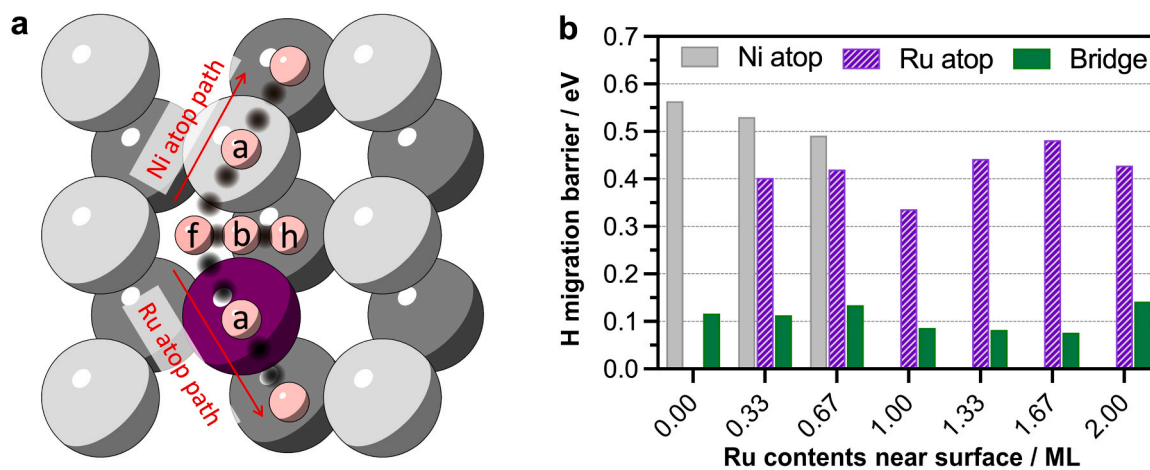


Fig. 6. (a) The low energy H diffusion paths on fcc (111) surface. Light and dark gray spheres are Ni atoms on the surface and sub-surface layer, respectively. Pink and purple spheres represent H and Ru atoms, respectively. (b) The energy barrier for H migration through the Ni, Ru atom, and bridge sites. Gray, purple, and green bars represent the migration barriers through Ni, Ru atop, and bridging sites, respectively.

range of 2.3–1.35 V (Fig. 7). Spray-coated  $\text{IrO}_x$  on CP, Ti fiber felt, and Pt-coated Ti fiber felt were used as anodes, and Nafion 112 membrane was placed therebetween to prepare MEA. Fig. 7a shows the scheme of the PEMWE system in which the  $\text{Ni}_{98.1}\text{Ru}_{1.9}$  catalyst integrated electrode is applied as the cathode and  $\text{IrO}_x$  on Pt-coated Ti fiber felt is applied as the anode. As a result, the  $\text{Ni}_{98.1}\text{Ru}_{1.9}/\text{CP}$  cathode-embedded PEMWE exhibited a performance of  $0.737 \text{ A cm}^{-2}$  at  $1.7 \text{ V}_{\text{cell}}$ , which is about half of that of Pt ( $0.1 \text{ mg of Pt per cm}^2$ )/C/CP cathode-embedded PEMWE ( $1.515 \text{ A cm}^{-2}$ ), while it exhibited excellent performance of  $3.2 \text{ A cm}^{-2}$ , comparable to PEMWE with Pt/C ( $3.36 \text{ A cm}^{-2}$ ) at  $2.0 \text{ V}_{\text{cell}}$ . The performance of PEMWE with  $\text{Ni}_{98.1}\text{Ru}_{1.9}$  outperformed that with Pt/C after  $2 \text{ V}_{\text{cell}}$  and displayed 1.45 times greater performance ( $6.53 \text{ A cm}^{-2}$ ) than Pt/C ( $4.5 \text{ A cm}^{-2}$ ) at  $2.3 \text{ V}_{\text{cell}}$  due to the significant mass transport resistance of powder type catalysts in high voltage/current environments when compared to that of catalyst-integrated electrode [81,82]. In addition, further comparison has been made for the PEMWE having similar amounts of Pt/C ( $0.05 \text{ mg of Pt per cm}^2$ ) with Ru exhibiting much lower performance of  $2.51 \text{ A cm}^{-2}$  at  $2.3 \text{ V}_{\text{cell}}$  (Fig. S17a). Thicker

membrane of Nafion 115 membrane was also tested to identify the effects of membrane thickness on the PEMWE performances (Fig. S17b). Similar trend in the performances according to the types of cathodes was maintained while the overall performances and differences among the samples were decreased because the large ohmic resistances from the thicker membrane dominated the other effects. For a more precise understanding the performance behaviors, activation, ohmic, and mass transport overpotentials were subdivided by Tafel analysis with resistances obtained from the EIS measurement (Fig. S18) and presented in Fig. 7c and d for PEMWEs with Pt/C/CP and  $\text{Ni}_{98.1}\text{Ru}_{1.9}/\text{CP}$  cathodes, respectively. The most significant differences between the two PEMWEs were the overpotentials related to mass transport observed at current densities higher than  $2 \text{ A cm}^{-2}$ . While the ohmic and activation overpotentials of PEMWE with  $\text{Ni}_{98.1}\text{Ru}_{1.9}/\text{CP}$  cathode are slightly higher than that with Pt/C/CP cathode, the mass transport overpotential was substantially smaller in PEMWE with  $\text{Ni}_{98.1}\text{Ru}_{1.9}/\text{CP}$  cathode giving a much higher performance at high current operation region. When  $\text{IrO}_x$  anode catalysts were formed on Ti fiber felt without Pt coating, the

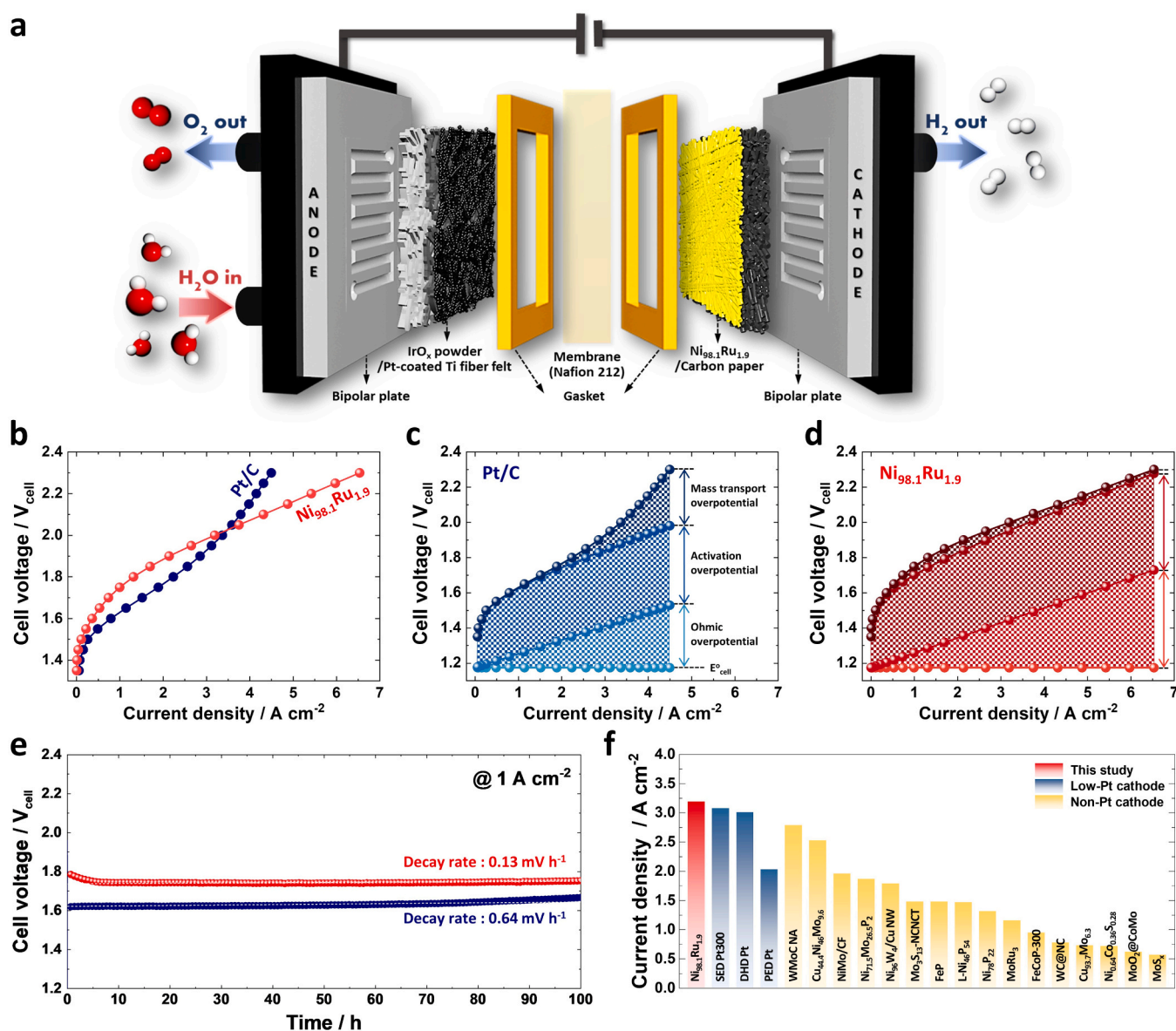


Fig. 7. (a) Schematic illustration of the PEMWE system with  $\text{Ni}_{98.1}\text{Ru}_{1.9}$  porous transport electrode (PTE). (b) Single-cell polarization curves using  $\text{Ni}_{98.1}\text{Ru}_{1.9}/\text{CP}$  ( $0.046 \text{ mg of Ru per cm}^2$ ) and Pt/C/CP ( $0.1 \text{ mg of Pt per cm}^2$ ) cathodes. Overpotential subdivisions for (c) Pt/C/CP and (d)  $\text{Ni}_{98.1}\text{Ru}_{1.9}/\text{CP}$  cathodes. (e) Long-term stability at a current density of  $1 \text{ A cm}^{-2}$  for 100 h. (f) Performance comparison of our PEMWE with those reported in the literature using current density at  $2.0 \text{ V}_{\text{cell}}$  as presented in Table S5 and S6.

performances of PEMWEs were decreased regardless of the cathode types (Fig. S19a) due to the increase in ohmic resistance caused by the oxidation of Ti [67,68] as shown in Fig. S18a. The durability of the electrode was tested by monitoring the cell voltage change for 100 h at a high current density of  $1 \text{ A cm}^{-2}$  (Fig. 7e). PEMWE with a commercial Pt/C/CP cathode exhibited a stable operation overall, but gradually deteriorated with a decay rate of  $0.64 \text{ mV h}^{-1}$ . Our  $\text{Ni}_{98.1}\text{Ru}_{1.9}/\text{CP}$  cathode-adopted PEMWE exhibited an initial activation (performance increase exhibiting cell voltage decrease) for roughly 6 h, and then maintained a very stable behavior with an overall decay rate of  $0.13 \text{ mV h}^{-1}$  from 6 h until 100 h, with superior stability than the one with commercial Pt/C cathode. After the durability test for 100 h, the dissolution of catalysts in the electrode was evaluated by ICP-MS. The original amounts of Ni ( $1.35 \text{ mg cm}^{-2}$ ) and Ru ( $0.046 \text{ mg cm}^{-2}$ ) in the as-made electrode have been somewhat dissolved at this high current single cell operation for 100 h, remaining  $0.918 \text{ mg cm}^{-2}$  of Ni and  $0.019 \text{ mg cm}^{-2}$  of Ru. Unlike the half-cell durability test,  $1 \text{ A cm}^{-2}$  operation resulted in about 32.0% and 58.7% of dissolution, respectively. However, the remaining Ni and Ru maintain the atomic ratio of  $\text{Ni}_{98.8}\text{Ru}_{1.2}$ , which is very close to  $\text{Ni}_{98.9}\text{Ru}_{1.1}$  that has almost identical high specific activity to  $\text{Ni}_{98.1}\text{Ru}_{1.9}$  in Fig. 3e. This explains the stability of the electrode even after 100 h high current operation. Similar to the performance behavior, when  $\text{IrO}_x$  anode catalysts were formed on Ti fiber felt without Pt coating, it showed faster decay rates of  $3.24 \text{ mV h}^{-1}$  for Pt/C and  $0.42 \text{ mV h}^{-1}$  for  $\text{Ni}_{98.1}\text{Ru}_{1.9}$  as presented in Fig. S19b. The obtained single cell performance was compared with literature-reported results in terms of the current density at  $2 V_{\text{cell}}$  in Fig. 7f. Since many factors such as electrode materials, membrane, operating temperature may affect the cell performance, the detailed conditions of each case were described in Table S5 (non-Pt cathodes) and S6 (low Pt cathodes). The performance of PEMWE with  $\text{Ni}_{98.1}\text{Ru}_{1.9}$  at  $2 V_{\text{cell}}$  ( $3.2 \text{ A cm}^{-2}$ ) outperformed the reported PEMWE with non-Pt cathodes ( $0.62\text{--}2.789 \text{ A cm}^{-2}$  at  $2 V_{\text{cell}}$ ). Moreover, our  $\text{Ni}_{98.1}\text{Ru}_{1.9}$  cathode-adopted PEMWE demonstrated a performance on par with or better than those with low-Pt ( $2.031\text{--}3.08 \text{ A cm}^{-2}$  at  $2 V_{\text{cell}}$ ) cathodes, implying that  $\text{Ni}_{98.1}\text{Ru}_{1.9}/\text{CP}$  is an economical electrode with Pt-like performance. There are many literatures using CP as the PTL of the anode since CP shows a higher performance because of its better conductivity. However, carbon oxidation may cause issues in long-term stability unless the carbon fibers are completely coated with catalysts [9]. We also tested CP as the anode PTL, and the PEMWE with  $\text{Ni}_{98.1}\text{Ru}_{1.9}/\text{CP}$  cathode and  $\text{IrO}_x/\text{CP}$  anode exhibited a slightly higher performance of  $3.45 \text{ A cm}^{-2}$  at  $2 V_{\text{cell}}$  but poorer durability with a decay rate of  $1.62 \text{ mV h}^{-1}$  (Fig. S20). From half-cell HER assessment to single-cell level verification, our  $\text{Ni}_{98.1}\text{Ru}_{1.9}$  electrode has demonstrated tremendous potential as an alternative to Pt in water electrolysis systems for the future hydrogen-economic society.

#### 4. Conclusions

As a low cost, high activity and durable HER catalyst, Ni PTE with trace amounts of Ru dopant was designed and fabricated by a simple one-step electrodeposition method on carbon paper PTL. The amount of Ru doping was finely tuned by Ru-ligand complex induced kinetic-retarded electrodeposition. From various spectroscopic analysis including XAS, the resulting catalysts have film-like structured nanocrystalline with surface-enriched Ru having atomically dispersed Ni-Ru bond coordination. While  $\text{Ni}_{100}$  showed almost no performance against acidic HER due to its strong hydrogen adsorption strength,  $\text{Ni}_{98.1}\text{Ru}_{1.9}$  catalyst with Ru contents less than  $0.05 \text{ mg}$  of Ru per  $\text{cm}^2$  exhibited a high performance of  $35 \text{ mV}$  at  $-10 \text{ mA cm}^{-2}$ . DFT calculation revealed that Ru doping on Ni surface decreased the hydrogen adsorption strength and facilitated the hydrogen mobility on the surface, enhancing the HER activity. In contrast to the rapid increase in the overpotential by  $60 \text{ mV}$  in  $\text{Ru}_{100}$  catalyst during the half-cell durability evaluation for 24 h,  $\text{Ni}_{98.1}\text{Ru}_{1.9}$  showed excellent durability with no noticeable

potential change, suggesting the stability of atomically dispersed Ru within the Ni lattice. By adopting the  $\text{Ni}_{98.1}\text{Ru}_{1.9}/\text{CP}$  directly to the cathode of PEMWE, it showed excellent performance of  $3.2 \text{ A cm}^{-2}$  comparable to that with Pt/C/CP ( $3.36 \text{ A cm}^{-2}$  with  $0.1 \text{ mg}$  of Pt per  $\text{cm}^2$ ) cathode at  $2 V_{\text{cell}}$ . The performance was even better at higher current region ( $6.0 \text{ A cm}^{-2}$  and  $4.3 \text{ A cm}^{-2}$  for  $\text{Ni}_{98.1}\text{Ru}_{1.9}/\text{CP}$  and Pt/C/CP at  $2.25 V_{\text{cell}}$ , respectively) due to the beneficial electrode structure to mass transport, outperforming the previously reported non-Pt cathodes and low Pt cathodes. In addition to its high performance, the extremely stable durability of  $\text{Ni}_{98.1}\text{Ru}_{1.9}/\text{CP}$ -embedded PEMWE ( $0.13 \text{ mV h}^{-1}$  decay rate for 100 h at  $1 \text{ A cm}^{-2}$ ) demonstrates its readiness as a highly active, durable, and cheap cathode for PEMWE.

#### CRedit authorship contribution statement

**Kim Hoyoung:** Conceptualization, Data curation, Investigation, Methodology, Writing – original draft. **Lee Kug-Seung:** Data curation, Formal analysis, Investigation, Funding acquisition. **Yeo Kyeong-Rim:** Conceptualization, Formal analysis, Investigation, Methodology, Writing – original draft. **Lee Jinwoo:** Conceptualization, Investigation, Methodology, Supervision, Validation, Writing – review & editing, Funding acquisition. **Park Haesun:** Conceptualization, Data curation, Investigation, Methodology, Software, Writing – review & editing. **Kim Soo-Kil:** Conceptualization, Funding acquisition, Investigation, Methodology, Project administration, Supervision, Validation, Writing – review & editing. **Kim Seongbeen:** Data curation, Formal analysis.

#### Declaration of Competing Interest

The authors declare that they have no known competing financial interests or personal relationships that could have appeared to influence the work reported in this paper.

#### Data availability

Data will be made available on request.

#### Acknowledgments

This work was supported by the National Research Foundation of Korea (NRF) grant funded by the Korean government (MSIT) (grant number: 2021R1A2C1005636, 2022M3I3A1081901, RS-2023-00235596, and 2019M3D1A1079309).

#### Appendix A. Supporting information

Supplementary data associated with this article can be found in the online version at [doi:10.1016/j.apcatb.2024.123738](https://doi.org/10.1016/j.apcatb.2024.123738).

#### References

- [1] S. Jiao, X. Fu, S. Wang, Y. Zhao, Perfecting electrocatalysts via imperfections: towards the large-scale deployment of water electrolysis technology, *Energy Environ. Sci.* 14 (2021) 1722–1770, <https://doi.org/10.1039/D0EE03635H>.
- [2] T. Terlouw, C. Bauer, R. McKenna, M. Mazzotti, Large-scale hydrogen production via water electrolysis: a techno-economic and environmental assessment, *Energy Environ. Sci.* 15 (2022) 3583–3602, <https://doi.org/10.1039/D2EE01023B>.
- [3] M. Carmo, D.L. Fritz, J. Mergerl, D. Stolten, A comprehensive review on PEM water electrolysis, *Int. J. Hydrog. Energy* 38 (2013) 4901–4934, <https://doi.org/10.1016/j.ijhydene.2013.01.151>.
- [4] S. Shiva Kumar, V. Himabindu, Hydrogen production by PEM water electrolysis – a review, *Mater. Sci. Energy Tech.* 2 (2019) 442–454, <https://doi.org/10.1016/j.mset.2019.03.002>.
- [5] M. Chatnet, B.G. Pollet, D.R. Dekel, F. Dionigi, J. Deseure, P. Millet, R.D. Braatz, M. Z. Bazant, M. Eikerling, I. Staffell, P. Balcombe, Y. Shao-Horn, H. Schäfer, Water electrolysis: from textbook knowledge to the latest scientific strategies and industrial developments, *Chem. Soc. Rev.* 51 (2022) 4583–4762, <https://doi.org/10.1039/D0CS01079K>.
- [6] M. Bernt, A. Hartig-Weiß, M. Fathi Tovini, H.A. El-Sayed, C. Schramm, J. Schröter, C. Gebauer, H.A. Gasteiger, Current challenges in catalyst development for PEM

- water electrolyzers, *Chem. Ing. Tech.* 92 (2020) 31–39, <https://doi.org/10.1002/cite.201900101>.
- [7] C. Minke, M. Suermann, B. Bensmann, R. Hanke-Rauschenbach, Is iridium demand a potential bottleneck in the realization of large-scale PEM water electrolysis? *Int. J. Hydrog. Energy* 46 (2021) 23581–23590, <https://doi.org/10.1016/j.ijhydene.2021.04.174>.
- [8] B.-S. Lee, S.H. Ahn, H.-Y. Park, I. Choi, S.J. Yoo, H.-J. Kim, D. Henkensmeier, J. Y. Kim, S. Park, S.W. Nam, K.-Y. Lee, J.H. Jang, Development of electrodeposited IrO<sub>2</sub> electrodes as anodes in polymer electrolyte membrane water electrolysis, *Appl. Catal. B-Environ.* 179 (2015) 285–291, <https://doi.org/10.1016/j.apcatb.2015.05.027>.
- [9] K.-R. Yeo, K.-S. Lee, H. Kim, J. Lee, S.-K. Kim, A highly active and stable 3D dandelion spore-structured self-supporting Ir-based electrocatalyst for proton exchange membrane water electrolysis fabricated using structural reconstruction, *Energy Environ. Sci.* 15 (2022) 3449–3461, <https://doi.org/10.1039/D2EE01042A>.
- [10] H.-Y. Jeong, J. Oh, G.S. Yi, H.-Y. Park, S.K. Cho, J.H. Jang, S.J. Yoo, H.S. Park, High-performance water electrolyzer with minimum platinum group metal usage: Iron nitride-iridium oxide core-shell nanostructures for stable and efficient oxygen evolution reaction, *Appl. Catal. B-Environ.* 330 (2023) 122596, <https://doi.org/10.1016/j.apcatb.2023.122596>.
- [11] X. Peng, P. Satjaritanun, Z. Taie, L. Wiles, A. Keane, C. Capuano, I.V. Zenyuk, N. Danilovic, Insights into interfacial and bulk transport phenomena affecting proton exchange membrane water electrolyzer performance at ultra-low iridium loadings, *Adv. Sci.* 8 (2021) 2102950, <https://doi.org/10.1002/adv.202102950>.
- [12] T. Lim, S.-K. Kim, Non-precious hydrogen evolution reaction catalysts: Stepping forward to practical polymer electrolyte membrane-based zero-gap water electrolyzers, *Chem. Eng. J.* 433 (2022) 133681, <https://doi.org/10.1016/j.cej.2021.133681>.
- [13] X. Zou, Y. Zhang, Noble metal-free hydrogen evolution catalysts for water splitting, *Chem. Soc. Rev.* 44 (2015) 5148–5180, <https://doi.org/10.1039/C4CS00448E>.
- [14] E.J. Popczun, J.R. McKone, C.G. Read, A.J. Biacchi, A.M. Wilttrout, N.S. Lewis, R. E. Schaak, Nanostructured nickel phosphide as an electrocatalyst for the hydrogen evolution reaction, *J. Am. Chem. Soc.* 135 (2013) 9267–9270, <https://doi.org/10.1021/ja403440e>.
- [15] H. Kim, E. Hwang, H. Park, B.-S. Lee, J.H. Jang, H.-J. Kim, S.H. Ahn, S.-K. Kim, Non-precious metal electrocatalysts for hydrogen production in proton exchange membrane water electrolyzer, *Appl. Catal. B-Environ.* 206 (2017) 608–616, <https://doi.org/10.1016/j.apcatb.2017.01.074>.
- [16] J. Kibsgaard, C. Tsai, K. Chan, J.D. Benck, J.K. Nørskov, F. Abild-Pedersen, T. F. Jaramillo, Designing an improved transition metal phosphide catalyst for hydrogen evolution using experimental and theoretical trends, *Energy Environ. Sci.* 8 (2015) 3022–3029, <https://doi.org/10.1039/C5EE02179K>.
- [17] J.K. Nørskov, T. Bligaard, A. Logadottir, J.R. Kitchin, J.G. Chen, S. Pandalov, U. Stimming, Trends in the exchange current for hydrogen evolution, *J. Electrochem. Soc.* 152 (2005) J23–J26, <https://doi.org/10.1149/1.1856988>.
- [18] C.C.L. McCrory, S. Jung, I.M. Ferrer, S.M. Chatman, J.C. Peters, T.F. Jaramillo, Benchmarking hydrogen evolving reaction and oxygen evolving reaction electrocatalysts for solar water splitting devices, *J. Am. Chem. Soc.* 137 (2015) 4347–4357, <https://doi.org/10.1021/ja510442p>.
- [19] K.J. Choi, H. Kim, S.-K. Kim, Multicomponent nonprecious hydrogen evolution catalysts for high performance and durable proton exchange membrane water electrolyzer, *J. Power Sources* 206 (2021) 230200, <https://doi.org/10.1016/j.jpowsour.2021.230200>.
- [20] P.M. Bodhankar, P.B. Sarawade, P. Kumar, A. Vinu, A.P. Kulkarni, C.D. Lokhande, D.S. Dhawale, Nanostructured metal phosphide based catalysts for electrochemical water splitting: a review, *Small* 18 (2022) 2107572, <https://doi.org/10.1002/smll.202107572>.
- [21] L. Lin, P. Sherrell, Y. Liu, W. Lei, S. Zhang, H. Zhang, G.G. Wallace, J. Chen, Engineered 2D transition metal dichalcogenides—a vision of viable hydrogen evolution reaction catalysis, *Adv. Energy Mater.* 28 (2020) 1903870, <https://doi.org/10.1002/aenm.201903870>.
- [22] Y. Wang, Y. Zhao, X. Ding, L. Qiao, Recent advances in the electrochemistry of layered post-transition metal chalcogenide nanomaterials for hydrogen evolution reaction, *J. Energy Chem.* 60 (2021) 451–479, <https://doi.org/10.1016/j.ijechem.2021.01.021>.
- [23] Q. Gao, W. Zhang, Z. Shi, L. Yang, Y. Tang, Structural design and electronic modulation of transition-metal-carbide electrocatalysts toward efficient hydrogen evolution, *Adv. Mater.* 31 (2019) 1802880, <https://doi.org/10.1002/adma.201802880>.
- [24] J. Theerthagiri, S.J. Lee, A.P. Murthy, J. Madhavan, M.Y. Choi, Fundamental aspects and recent advances in transition metal nitrides as electrocatalysts for hydrogen evolution reaction: a review, *Curr. Opin. Solid State Mater. Sci.* 24 (2020) 100805, <https://doi.org/10.1016/j.cossms.2020.100805>.
- [25] J. Park, H. Kim, G.H. Han, J. Kim, S.J. Yoo, H.-J. Kim, S.H. Ahn, Electrochemically fabricated MoO<sub>3</sub>-MoO<sub>2</sub>@NiMo heterostructure catalyst with Pt-like activity for the pH-universal hydrogen evolution reaction, *J. Mater. Chem. A* 9 (2021) 3677–3684, <https://doi.org/10.1039/D0TA08432H>.
- [26] J.H. Kim, J. Kim, H. Kim, J. Kim, S.H. Ahn, Facile fabrication of nanostructured NiMo cathode for high-performance proton exchange membrane water electrolyzer, *J. Ind. Eng. Chem.* 79 (2019) 255–260, <https://doi.org/10.1016/j.jiec.2019.06.049>.
- [27] J.R. McKone, B.F. Sadtler, C.A. Werlang, N.S. Lewis, H.B. Gray, Ni–Mo nanopowders for efficient electrochemical hydrogen evolution, *ACS Catal.* 3 (2013) 166–169, <https://doi.org/10.1021/cs300691m>.
- [28] H. Kim, H. Park, D.-K. Kim, S. Oh, I. Choi, S.-K. Kim, Electrochemically fabricated NiW on a Cu nanowire as a highly porous non-precious-metal cathode catalyst for a proton exchange membrane water electrolyzer, *ACS Sustain. Chem. Eng.* 7 (2019) 8265–8273, <https://doi.org/10.1021/acsuschemeng.8b06643>.
- [29] D. Gao, J. Guo, H. He, P. Xiao, Y. Zhang, Geometric and electronic modulation of fcc NiCo alloy by Group-VI B metal doping to accelerate hydrogen evolution reaction in acidic and alkaline media, *Chem. Eng. J.* 430 (2022) 133110, <https://doi.org/10.1016/j.cej.2021.133110>.
- [30] W.A. Badawy, H. Nady, M. Negem, Cathodic hydrogen evolution in acidic solutions using electrodeposited nano-crystalline Ni–Co cathodes, *Int. J. Hydrog. Energy* 39 (2014) 10824–10832, <https://doi.org/10.1016/j.ijhydene.2014.05.049>.
- [31] X.-D. He, F. Xu, F. Li, L. Liu, Y. Wang, N. Deng, Y.-W. Zhu, J.-B. He, Composition-performance relationship of Ni<sub>2</sub>Cu<sub>3</sub> nanoalloys as hydrogen evolution electrocatalyst, *J. Electroanal. Chem.* 799 (2017) 235–241, <https://doi.org/10.1016/j.jelechem.2017.05.050>.
- [32] Y. Pan, Y. Liu, J. Zhao, K. Yang, J. Liang, D. Liu, W. Hu, D. Liu, Y. Liu, C. Liu, Monodispersed nickel phosphide nanocrystals with different phases: synthesis, characterization and electrocatalytic properties for hydrogen evolution, *J. Mater. Chem. A* 3 (2015) 1656–1665, <https://doi.org/10.1039/C4TA04867A>.
- [33] H. Kim, H. Park, D.-K. Kim, I. Choi, S.-K. Kim, Pulse-electrodeposited nickel phosphide for high-performance proton exchange membrane water electrolysis, *J. Alloy. Compd.* 785 (2019) 296–304, <https://doi.org/10.1016/j.jallcom.2019.01.192>.
- [34] S. Anantharaj, S. Kundu, S. Noda, Progress in nickel chalcogenide electrocatalyzed hydrogen evolution reaction, *J. Mater. Chem. A* 8 (2020) 4174–4192, <https://doi.org/10.1039/C9TA14037A>.
- [35] H. Fan, H. Yu, Y. Zhang, Y. Zheng, Y. Luo, Z. Dai, B. Li, Y. Zong, Q. Yan, Fe-doped Ni<sub>3</sub>C nanodots in N-doped carbon nanosheets for efficient hydrogen-evolution and oxygen-evolution electrocatalysis, *Angew. Chem. Int. Ed.* 56 (2017) 12566–12570, <https://doi.org/10.1002/anie.201706610>.
- [36] J. Yin, Q. Fan, Y. Li, F. Cheng, P. Zhou, P. Xi, S. Sun, Ni–C–N nanosheets as catalyst for hydrogen evolution reaction, *J. Am. Chem. Soc.* 138 (2016) 14546–14549, <https://doi.org/10.1021/jacs.6b09351>.
- [37] D. Gao, J. Zhang, T. Wang, W. Xiao, K. Tao, D. Xue, J. Ding, Metallic Ni<sub>3</sub>N nanosheets with exposed active surface sites for efficient hydrogen evolution, *J. Mater. Chem. A* 4 (2016) 17363–17369, <https://doi.org/10.1039/C6TA07883D>.
- [38] Y. Yang, Y. Yu, J. Li, Q. Chen, Y. Du, P. Rao, R. Li, C. Jia, Z. Kang, P. Deng, Y. Shen, X. Tian, Engineering ruthenium-based electrocatalysts for effective hydrogen evolution reaction, *Nano-Micro Lett.* 13 (2021) 160, <https://doi.org/10.1007/s40820-021-00679-3>.
- [39] G. Chen, T. Wang, J. Zhang, P. Liu, H. Sun, X. Zhuang, M. Chen, X. Feng, Accelerated hydrogen evolution kinetics on NiFe-layered double hydroxide electrocatalysts by tailoring water dissociation active sites, *Adv. Mater.* 30 (2018) 1706279, <https://doi.org/10.1002/adma.201706279>.
- [40] J. Zhang, G. Chen, Q. Liu, C. Fan, D. Sun, Y. Tang, H. Sun, X. Feng, Competitive adsorption: reducing the poisoning effect of adsorbed hydroxyl on Ru single-atom site with SnO<sub>2</sub> for efficient hydrogen evolution, *Angew. Chem. Int. Ed.* 61 (2022) e202209486, <https://doi.org/10.1002/anie.202209486>.
- [41] T. Qiu, Z. Liang, W. Guo, S. Gao, C. Qu, H. Tabassum, H. Zhang, B. Zhu, R. Zou, Y. Shao-Horn, Highly exposed ruthenium-based electrocatalysts from bimetallic metal-organic frameworks for overall water splitting, *Nano Energy* 58 (2019) 1–10, <https://doi.org/10.1016/j.nanoen.2018.12.085>.
- [42] J. Mahmood, F. Li, S.M. Jung, M.S. Okyay, I. Ahmad, S.J. Kim, N. Park, H.Y. Jeong, J.B. Baek, An efficient and pH-universal ruthenium-based catalyst for the hydrogen evolution reaction, *Nat. Nanotechnol.* 12 (2017) 441–446, <https://doi.org/10.1038/nnano.2016.304>.
- [43] T. Feng, G. Yu, S. Tao, S. Zhu, R. Ku, R. Zhang, Q. Zeng, M. Yang, Y. Chen, W. Chen, W. Chen, B. Yang, A highly efficient overall water splitting ruthenium-cobalt alloy electrocatalyst across a wide pH range via electronic coupling with carbon dots, *J. Mater. Chem. A* 8 (2020) 9638–9645, <https://doi.org/10.1039/D0TA02496A>.
- [44] Z. Zhang, P. Li, Q. Feng, Y. Tao, J. Xu, C. Jiang, X. Lu, J. Fan, M. Gu, H. Li, H. Wang, Mo modulation effect on the hydrogen binding energy of hexagonal-close-packed Ru for hydrogen evolution, *J. Mater. Chem. A* 7 (2019) 2780–2786, <https://doi.org/10.1039/C8TA11251G>.
- [45] Z. Pu, I.S. Amini, Z. Kou, W. Li, S. Mu, RuP<sub>2</sub>-based catalysts with platinum-like activity and higher durability for the hydrogen evolution reaction at all pH values, *Angew. Chem. Int. Ed.* 56 (2017) 11559–11564, <https://doi.org/10.1002/anie.201704911>.
- [46] Z. Zhang, C. Jiang, P. Li, K. Yao, Z. Zhao, J. Fan, H. Li, H. Wang, Benchmarking phases of ruthenium dichalcogenides for electrocatalysis of hydrogen evolution: theoretical and experimental insights, *Small* 17 (2021) 2007333, <https://doi.org/10.1002/smll.202007333>.
- [47] [metalsdaily.com/live-prices/pgms/](https://metalsdaily.com/live-prices/pgms/)
- [48] C.-Y. Ahn, J.E. Park, S. Kim, O.-H. Kim, W. Hwang, M. Her, S.Y. Kang, S.B. Park, O. J. Kwon, H.S. Park, Y.-H. Cho, Y.-E. Sung, Differences in the electrochemical performance of Pt-based catalysts used for polymer electrolyte membrane fuel cells in liquid half- and full-cells, *Chem. Rev.* 121 (2021) 15075–15140, <https://doi.org/10.1021/acs.chemrev.0c1337>.
- [49] K. Ehelebe, D. Escalera-López, S. Cherevko, Limitations of aqueous model systems in the stability assessment of electrocatalysts for oxygen reactions in fuel cell and electrolyzers, *Curr. Opin. Electrochem.* 29 (2021) 100832, <https://doi.org/10.1016/j.coelec.2021.100832>.
- [50] M.F. Lagadee, A. Grimaud, Water electrolyzers with closed and open electrochemical systems, *Nat. Mater.* 19 (2020) 1140–1150, <https://doi.org/10.1038/s41563-020-0788-3>.

- [51] M.B. Kale, R.A. Borse, A. Gomaa Abdelkader Mohamed, Y. Wang, Electrocatalysts by electrodeposition: recent advances, synthesis methods, and applications in energy conversion, *Adv. Funct. Mater.* 31 (2021) 2101313, <https://doi.org/10.1002/adfm.202101313>.
- [52] K.-R. Yeo, J. Eo, M.J. Kim, S.-K. Kim, Shape control of metal nanostructures by electrodeposition and their applications in electrocatalysis, *J. Electrochem. Soc.* 169 (2022) 112502, <https://doi.org/10.1149/1945-7111/ac9e21>.
- [53] A. Rasheed, J.Y. Howe, M.D. Dadmun, P.F. Britt, The efficiency of the oxidation of carbon nanofibers with various oxidizing agents, *Carbon* 45 (2007) 1072–1080, <https://doi.org/10.1016/j.carbon.2006.12.010>.
- [54] C.M. Elson, L.J. Itzkovitch, J. Mckenney, J.A. Page, Electrochemistry of ruthenium ammine complexes, *Can. J. Chem.* 53 (1975) 2922–2929, <https://doi.org/10.1139/v75-413>.
- [55] M. Supicova, R. Rozik, L. Trnkova, R. Orinakova, M. Galova, Influence of boric acid on the electrochemical deposition of Ni, *J. Solid. State Electrochem.* 10 (2006) 61–68, <https://doi.org/10.1007/s10008-005-0656-8>.
- [56] V.R. Stamenkovic, B.S. Mun, M. Arenz, K.J. Mayrhofer, C.A. Lucas, G. Wang, P. N. Ross, N.M. Markovic, Trends in electrocatalysis on extended and nanoscale Pt-bimetallic alloy surfaces, *Nat. Mater.* 6 (2007) 241–247, <https://doi.org/10.1038/nmat1840>.
- [57] H. Magai, E. Shibata, T. Nakamura, Recovery of ruthenium from a solution containing platinum group metals, *J. Jpn. I. Met. Mater.* 81 (2017) 178–185, <https://doi.org/10.2320/jinstmet.JE201606>.
- [58] P. Hohenberg, W. Kohn, Inhomogeneous electron gas, *Phys. Rev.* 136 (1964) B864–B871, <https://doi.org/10.1103/PhysRev.136.B864>.
- [59] G. Kresse, J. Furthmüller, Efficient iterative schemes for ab initio total-energy calculations using a plane-wave basis set, *Phys. Rev. B* 54 (1996) 11169–11186, <https://doi.org/10.1103/PhysRevB.54.11169>.
- [60] P.E. Blöchl, Projector augmented-wave method, *Phys. Rev. B* 50 (1994) 17953–17979, <https://doi.org/10.1103/PhysRevB.50.17953>.
- [61] G. Kresse, D. Joubert, From ultrasoft pseudopotentials to the projector augmented-wave method, *Phys. Rev. B* 59 (1999) 1758–1775, <https://doi.org/10.1103/PhysRevB.59.1758>.
- [62] J.P. Perdew, K. Burke, M. Ernzerhof, Generalized gradient approximation made simple, *Phys. Rev. Lett.* 77 (1996) 3865–3868, <https://doi.org/10.1103/PhysRevLett.77.3865>.
- [63] S.P. Ong, W.D. Richards, A. Jain, G. Hautier, M. Kocher, S. Cholia, D. Gunter, V. L. Chevrier, K.A. Persson, G. Ceder, Python Materials Genomics (pymatgen): a robust, open-source python library for materials analysis, *Comput. Mater. Sci.* 68 (2013) 314–319, <https://doi.org/10.1016/j.commatsci.2012.10.028>.
- [64] G. Henkelman, A. Arnaldsson, H. Jónsson, A fast and robust algorithm for Bader decomposition of charge density, *Comput. Mater. Sci.* 36 (2006) 354–360, <https://doi.org/10.1016/j.commatsci.2005.04.010>.
- [65] W. Tang, E. Sanville, G. Henkelman, A grid-based Bader analysis algorithm without lattice bias, *J. Phys. -Condens. Matter* 21 (2009) 084204, <https://doi.org/10.1088/0953-8984/21/8/084204>.
- [66] G. Henkelman, D.P. Uberuaga, H. Jónsson, A climbing image nudged elastic band method for finding saddle points and minimum energy paths, *J. Chem. Phys.* 113 (2000) 9901–9904, <https://doi.org/10.1063/1.1329672>.
- [67] C. Rakousky, U. Reimer, K. Wippermann, M. Carmo, W. Lueke, D. Stolten, An analysis of degradation phenomena in polymer electrolyte membrane water electrolysis, *J. Power Sources* 326 (2016) 120–128, <https://doi.org/10.1016/j.jpowsour.2016.06.082>.
- [68] C. Liu, M. Shviro, A.S. Gago, S.F. Zaccarine, G. Bender, P. Gazdzicki, T. Morawietz, I. Biswas, M. Rasinski, A. Everwand, R. Schierholz, J. Pfeilsticker, M. Müller, P. P. Lopes, R.-A. Eichel, B. Pivovar, S. Pylypenko, K.A. Friedrich, W. Lehnert, M. Carmo, Exploring the interface of skin-layered titanium fibers for electrochemical water splitting, *Adv. Energy Mater.* 11 (2021) 2002926, <https://doi.org/10.1002/aenm.202002926>.
- [69] C.A. Marozzi, A.C. Chialvo, Development of electrode morphologies of interest in electrocatalysis. Part 1: electrodeposited porous nickel electrodes, *Electrochim. Acta* 45 (2000) 2111–2120, [https://doi.org/10.1016/S0013-4686\(99\)00422-3](https://doi.org/10.1016/S0013-4686(99)00422-3).
- [70] H. Funke, A.C. Scheinost, M. Chukalina, Wavelet analysis of extended x-ray absorption fine structure data, *Phys. Rev. B* 71 (2005) 094110, <https://doi.org/10.1103/PhysRevB.71.094110>.
- [71] H. Prats, K. Chan, The determination of the HOR/HER reaction mechanism from experimental kinetic data, *Phys. Chem. Chem. Phys.* 23 (2021) 27150–27158, <https://doi.org/10.1039/D1CP04134G>.
- [72] A. Lasia, Mechanism and kinetics of the hydrogen evolution reaction, *Int. J. Hydrog. Energy* 44 (2019) 19484–19518, <https://doi.org/10.1016/j.ijhydene.2019.05.183>.
- [73] P.A. Allen, A. Hickling, Electrochemistry of sulphur. Part 1.—overpotential in the discharge of the sulphide ion, *Trans. Faraday Soc.* 53 (1957) 1626–1635, <https://doi.org/10.1039/TF9575301626>.
- [74] A.J. Bard, L.R. Faulkner, *Electrochemical Methods: Fundamentals and Applications*, second ed., Wiley, 2000.
- [75] C.C.L. McCrory, S. Jung, J.C. Peters, T.F. Jaramillo, Benchmarking heterogeneous electrocatalysts for the oxygen evolution reaction, *J. Am. Chem. Soc.* 135 (2013) 16977–16987, <https://doi.org/10.1021/ja407115p>.
- [76] M.S. Hegde, T.S. Sampath Kumar, R.M. Mallya, XPS, UPS and AES study of surface segregation and oxidation of Ni-Ru alloy: evidence for decrease in dissociation temperature of NiO in the presence of Ru, *Surf. Sci.* 188 (1987) 255–266, [https://doi.org/10.1016/S0039-6028\(87\)80156-5](https://doi.org/10.1016/S0039-6028(87)80156-5).
- [77] B. Hammer, J.K. Nørskov, Why gold is the noblest of all the metals, *Nature* 376 (1995) 238–240, <https://doi.org/10.1038/376238a0>.
- [78] A. Ruban, B. Hammer, P. Stoltze, H.L. Skriver, J.K. Nørskov, Surface electronic structure and reactivity of transition and noble metals, *J. Mol. Catal. A-Chem.* 115 (1997) 421–429, [https://doi.org/10.1016/S1381-1169\(96\)00348-2](https://doi.org/10.1016/S1381-1169(96)00348-2).
- [79] J.R. Kitchin, J.K. Nørskov, M.A. Barteau, J.G. Chen, Role of strain and ligand effects in the modification of the electronic and chemical properties of bimetallic surfaces, *Phys. Rev. Lett.* 93 (2004) 156801, <https://doi.org/10.1103/PhysRevLett.93.156801>.
- [80] G.W. Watson, R.P.K. Wells, D.J. Willock, G.J. Hutchings, A comparison of the adsorption and diffusion of hydrogen on the {111} surfaces of Ni, Pd, and Pt from density functional theory calculations, *J. Phys. Chem. B* 105 (2001) 4889–4894, <https://doi.org/10.1021/jp002864c>.
- [81] H. Kim, S. Choe, H. Park, J.H. Jang, S.H. Ahn, S.-K. Kim, An extremely low Pt loading cathode for a highly efficient proton exchange membrane water electrolyzer, *Nanoscale* 9 (2017) 19045–19049, <https://doi.org/10.1039/C7NR07224D>.
- [82] H. Huang, H. Kim, A. Lee, S. Kim, W.-G. Lim, C.-Y. Park, S. Kim, S.-K. Kim, J. Lee, Structure engineering defective and mass transfer-enhanced RuO<sub>2</sub> nanosheets for proton exchange membrane water electrolyzer, *Nano Energy* 88 (2021) 106276, <https://doi.org/10.1016/j.nanoen.2021.106276>.